

NONLINEAR OPTICAL PROPERTIES OF SEMICONDUCTOR
HETEROSTRUCTURES

A THESIS SUBMITTED TO
THE GRADUATE SCHOOL OF NATURAL AND APPLIED SCIENCES
OF
MIDDLE EAST TECHNICAL UNIVERSITY

BY

HASAN YILDIRIM

IN PARTIAL FULFILLMENT OF THE REQUIREMENTS
FOR
THE DEGREE OF DOCTOR OF PHILOSOPHY
IN
PHYSICS

AUGUST 2006

Approval of the Graduate School of Natural and Applied Sciences.

Prof. Dr. Canan Özgen
Director

I certify that this thesis satisfies all the requirements as a thesis for the degree of Doctor of Philosophy.

Prof. Dr. Sinan Bilikmen
Head of Department

This is to certify that we have read this thesis and that in our opinion it is fully adequate, in scope and quality, as a thesis for the degree of Doctor of Philosophy.

Prof. Dr. Mehmet Tomak
Supervisor

Examining Committee Members

Prof. Dr. Yakup Cevdet Akgöz (METU, ES) _____

Prof. Dr. Mehmet Tomak (METU, PHYS) _____

Prof. Dr. Mehmet Parlak (METU, PHYS) _____

Assist. Prof. Dr. Ceyhun Bulutay (Bil. U., PHYS) _____

Assist. Prof. Dr. Sadi Turgut (METU, PHYS) _____

“I hereby declare that all information in this document has been obtained and presented in accordance with academic rules and ethical conduct. I also declare that, as required by these rules and conduct, I have fully cited and referenced all material and results that are not original to this work.”

Name, Last name : HASAN YILDIRIM

Signature :

ABSTRACT

NONLINEAR OPTICAL PROPERTIES OF SEMICONDUCTOR HETEROSTRUCTURES

Yıldırım, Hasan

Ph.D., Department of Physics

Supervisor: Prof. Dr. Mehmet Tomak

August 2006, 112 pages.

The nonlinear optical properties of semiconductor heterostructures, such as GaAs/ $\text{Al}_x\text{Ga}_{1-x}\text{As}$ alloys, are studied with analytic and numerical methods on the basis of quantum mechanics. Particularly, second and third-order nonlinear optical properties of quantum wells described by the various types of confining potentials are considered within the density matrix formalism. We consider a Pöschl-Teller type potential which has been rarely considered in this area. It has a tunable asymmetry parameter, making it a good candidate to investigate the effect of the asymmetry on the nonlinear optical properties. The calculated nonlinear quantities include nonlinear absorption coefficient, second-harmonic generation, optical rectification, third-harmonic generation and the intensity-dependent refractive index. The effect of the DC electric field on the corresponding nonlinearities are

also studied. The results are in good agreement with the results obtained in other types of quantum wells, such as square and parabolic quantum wells. The effect of the Coulomb interaction among the electrons on the nonlinear intersubband absorption are considered within the rotating wave approximation. The result is applied to a Si- δ -doped, square quantum well in which the Coulomb interaction among the electrons are relatively important, since there has been no work on the nonlinear absorption spectrum of the Si- δ -doped quantum well. The results are found to be new and interesting, especially when a DC electric field is included in the calculations.

Keywords: Quantum Wells, Pöschl-Teller potential, Intersubband transitions, Second-harmonic generation, Third-harmonic generation.

ÖZ

YARIİLETKEN HETEROYAPILARIN LİNEER OLMAYAN OPTİK
ÖZELLİKLERİ

Yıldırım, Hasan

Doktora, Fizik Bölümü

Tez Yöneticisi: Prof. Dr. Mehmet Tomak

Ağustos 2006, 112 sayfa.

Yarıiletken malzemelerden imal edilen hetero yapıların, özellikle GaAs/Al_xGa_{1-x}As alaşımlarının, doğrusal olmayan optik özellikleri kuantum mekaniği temel alınarak nümerik ve analitik olarak çalışıldı. Özellikle Pöschl-Teller tipi potansiyele sahip kuantum kuyularının ikinci ve üçüncü dereceden doğrusal olmayan optik özellikleri, yoğunluk matrisi formalizmi içinde kalınarak incelendi. Bu tip bir potansiyelin optik özellikleri literatürde çok az incelenmiştir. Ayrıca potansiyelin simetrisinden sapma derecesini belirleyen bir parametre setine sahip olması, bu potansiyeli asimetrinin doğrusal olmayan optik özellikler üzerine etkisini incelemek için kaçınılmaz bir aday yapmaktadır. Hesaplanan optik özellikler şunları kapsamaktadır: Doğrusal olmayan soğurma katsayısı, ikinci harmonik yaratım, optik düzeltme, üçüncü harmonik yaratım ve yoğunluğa bağlı kırılma

indeksi. Ayrıca, bahsi geçen özelliklerin elektriksel alan altında değişimleri de incelenmiştir. Sonuçlar, benzeri sistemler olan kare ve parabolik kuantum kuyuları ile karşılaştırılmıştır. Elektronlararası Coulomb etkileşiminin doğrusal olmayan soğurma katsayısı dönen dalga yaklaşımı içinde çalışılmıştır. Sonuçlar elektronlar arası Coulomb etkileşimin önemli olduğu Si- δ - ekilmiş kuantum kuyularına uygulanmıştır çünkü bu yapılarda sadece Coulomb etkileşiminin doğrusal olmayan soğurma katsayısına etkisi hatta, katsayının kendisi üzerine bile literatürde herhangi bir çalışma bulunamamıştır. Özellikle elektrik alan etkisi hesaba katıldığında sonuçlar yeni ve ilgi çekici çıkmaktadır.

Anahtar Kelimeler: Kuantum Kuyuları, Pöschl-Teller potansiyeli, Bandiçi geçişler, İkinci-harmonik yaratım, Üçüncü harmonik yaratım.

...al mio padre ed al suo padre

ACKNOWLEDGMENTS

I would firstly like to thank my supervisor Prof. Dr. Mehmet Tomak for his indispensable support, encouragement and guidance throughout the whole study. I would also like to thank all my friends, especially to Dr. Hasan Hüseyin Kart, for their valuable guidance during my thesis study. Furthermore, I am very much indebted to my family for their love.

TABLE OF CONTENTS

PLAGIARISM	iii
ABSTRACT	iv
ÖZ	vi
DEDICATION	viii
ACKNOWLEDGMENTS	viii
TABLE OF CONTENTS	x
CHAPTER	
1 INTRODUCTION	1
2 SEMICONDUCTOR QUANTUM WELLS	8
2.1 Introduction	8
2.2 General Properties of Heterostructures	8
2.3 Envelope Function Description	12
3 NONLINEAR OPTICS	24
3.1 Introduction	24
3.2 A Simple Description	24
3.3 Quantum-Mechanical Theory of Nonlinear Susceptibilities	26
3.4 Perturbation Solution of the Density Matrix Equation	28
4 PÖSCHL-TELLER POTENTIAL	33
4.1 Introduction	33

4.2	Pöschl-Teller Potential	33
4.3	Schrödinger equation with Pöschl-Teller Potential	34
4.4	Pöschl-Teller potential under a DC electric field	37
5	SECOND-ORDER NONLINEARITIES	43
5.1	Introduction	43
5.2	Second-Harmonic Generation	43
5.3	Second-Harmonic Generation in a Pöschl-Teller Quantum Well	48
5.4	Optical Rectification	54
6	THIRD-ORDER NONLINEARITIES	59
6.1	Introduction	59
6.2	Nonlinear Intersubband Absorption	60
6.3	Nonlinear Intersubband Absorption in a Pöschl-Teller Quantum Well	61
6.4	Quantum-Confined Stark Effect	65
6.5	Third-Harmonic Generation	66
6.6	Third-Harmonic Generation in a Pöschl-Teller Quantum Well	68
6.7	Intensity-Dependent Refractive Index	70
7	NONLINEAR INTERSUBBAND ABSORPTION OF δ -DOPED QUANTUM WELLS	75
7.1	Introduction	75
7.2	Electronic Structure of δ -Doped Quantum Wells	76
7.2.1	Theoretical Description	76
7.2.2	Numerical Procedure	78
7.2.3	Results and Discussion	80
7.3	Nonlinear Intersubband Absorption of δ -Doped Quantum Wells	84
7.3.1	Results and Discussion	89

8	CONCLUSION	98
	REFERENCES	104
	VITA	111

CHAPTER 1

INTRODUCTION

The quantum confinement of carriers in one dimensional potentials formed by thin semiconductor layers (e.g. $\sim 100 \text{ \AA}$) has attracted enormous interest for the past three decades. A fast development in the field has been achieved due to epitaxial crystal growth techniques such as molecular beam epitaxy, which provides atomic-layer control of layer thickness. These techniques allowed a flexibility in fabricating structures with various types of confining potentials, a process called band-gap engineering.

The simplest system under these circumstances is a quantum well, formed by sandwiching a thin semiconductor layer between other semiconductor layers, having a larger bandgap. Fig. (1.1) shows such a quantum well. Electrons and holes are confined in the conduction band and valence band, respectively. The confinement leads to the quantized energy levels along the growth direction. Optical transitions among the energy levels are possible. Transitions from energy levels in the valence band to ones in the conduction band are called interband

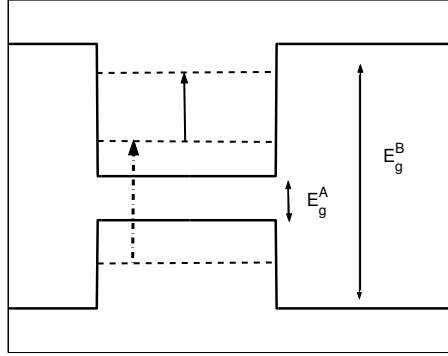


Figure 1.1: Schematic view of a simple quantum well and the optical transitions inside it. The solid arrow denotes the intersubband transitions while the dashed-dotted one shows the interband transitions. E_g^A and E_g^B are the respective band-gap energies of the semiconductors, constituting the heterostructures.

transitions whereas transitions among the energy levels in the same band are called intersubband transitions. The quantum well depth and thickness allow the energy levels, optical dipole matrix elements, populations and even the relaxation times to some extent to be tunable.

Dingle et al. [1] in 1974 observed the first experimental evidence for quantized states in a semiconductor quantum well. Their quantum well was a thin GaAs layer sandwiched between two $\text{Al}_x\text{Ga}_{1-x}\text{As}$ layers acting as barriers. The excitonic transitions associated with different electron and hole states were observed in the absorption spectra. The first experimental observation of the intersubband transitions in the conduction band of a GaAs/AlGaAs quantum well was presented by West and Eglash [2] although some earlier theoretical works showed

the possibility of infrared light detection based on the intersubband transitions in quantum wells [3, 4]. West and Eglash [2] observed transitions around $10\ \mu\text{m}$ having a narrow linewidth ($\sim 10\ \text{meV}$) and a large oscillator strength. Although in other quasi-two dimensional electron systems, such as accumulation and inversion layers, the intersubband transitions were showed earlier, the investigations attracted less interest in this field [5]. This is because the absorption wavelength in such structures occurred at far-infrared region ($\sim 40\ \mu\text{m}$) but the absorption in the experiment of West and Eglash [2] occurred in the technologically important region [5].

A great deal of effort has been devoted to the intersubband transitions in quantum wells, including not only GaAs/AlGaAs structures but also InGaAs/AlGaAs, InGaAs-InAlAs lattice matched to InP, and InAs-AlGaSb structures since 1985 [5]. Many device applications based on the intersubband absorption, like infrared detectors and emitters, have been suggested or realized [5].

Nonlinear optics has been an important field in physics since the discovery of second-harmonic generation by Franken *et al.* [6] in 1961. In their pioneering work, they discovered second-harmonic generation when they propagated a ruby laser beam at $6942\ \text{\AA}$ through a quartz crystal and observed ultraviolet radiation from the crystal at $3471\ \text{\AA}$. The discovery of second-harmonic generation shortly after the demonstration of the first working laser [7] was not accidental as only the laser light is intense enough to demonstrate the nonlinear optical properties

of materials. It is nonlinear because the response of the system to the applied optical field is a nonlinear function of the strength of the field. For example, the saturation of the intersubband absorption in a GaAs/AlGaAs quantum well depends on the square of the strength of the optical field. A more clear example is that third-harmonic generation depends upon the cubic power of the strength of the optical field.

A novel feature of the semiconductor quantum wells is that the dipole matrix element associated with the intersubband transitions in such structures have the same order of magnitude as the width of the quantum well. Since the nonlinear optical properties, like second-harmonic generation, depend on the higher powers of the dipole matrix elements, one can expect huge nonlinearities in semiconductor quantum wells. In fact, this was showed theoretically by Gurnick and DeTemple [8] in compositional asymmetric GaAs/AlGaAs quantum wells in 1983, where they obtained nonlinearities larger than those of bulk materials. In 1989, Fejer *et al.* [9] observed second-order nonlinearities in a biased GaAs/AlGaAs quantum well for the first time. Since the semiconductor quantum wells have controllable transition energies, dipole matrix elements and asymmetry by the band-gap engineering, their nonlinear optical properties have attracted a great interest [10, 11] since the works of Gurnick and DeTemple [8] and Fejer *et al.* [9]. In spite of such a enormous effort in the field, the usage of nonlinear optical properties of semiconductors in the frequency conversion is limited by difficulties in

efficient coupling of the pump power to the intersubband transitions, the strong absorption of the external pump power and the lack of a suitable phase-matching scheme in most III-V semiconductors [10, 11, 12].

The asymmetry of the confining potential in quantum wells play an important role in obtaining high values of nonlinear optical properties. In fact, the second-order nonlinearities are observed only in noncentrosymmetric structures, that is structures lacking an inversion symmetry. For example, equal energy spacings, the optimized dipole matrix elements and increased lifetimes achieved in stepped or asymmetric double quantum wells lead to huge resonant nonlinearities [10, 11, 13]. Generally, the asymmetric quantum wells used in the maximization of the optical nonlinearities have included biased square, stepped, double or triple quantum wells in the literature so far. However, these asymmetric forms are not flexible, they are rigid in shape. A variable asymmetry property in a quantum well thus will be very helpful to investigate the effects of the asymmetry on the nonlinear optical properties. The Pöschl-Teller potential is a good candidate for that investigation. It can easily be made asymmetric through a correct choice of its parameter set. Within the allowed range of the parameters, the potential has analytic solutions so that the nonlinearities can be evaluated analytically. This is exactly what we do in the first part of this thesis.

The Coulomb interaction among the carries in a quantum well leads to novel results in optics. Among them, one is the blue-shift of the peak position with

respect to bare intersubband transition energy in the absorption spectra at low intensities of the optical field, which is called the depolarization shift. Whereas, at higher intensities of the optical field, close to or higher than the saturation intensity, the Coulomb interaction not only shifts the peak position but also makes the absorption spectra asymmetric in an amount determined by the intensity of the optical field [14]. Our aim in the second part of the thesis is to apply the results developed by Załużny [14] to the calculations of the nonlinear intersubband absorption in a Si- δ -doped quantum wells which is a missing part in the absorption calculations of such structures in the literature because the electron density here is high enough to take into account the Coulomb interaction.

The thesis is organized as follows. We review the general properties of semiconductor heterostructures and give the basic idea behind the envelope function description of their electronic structure in Chapter 2. While there are several ways to describe the electronic band structure, the envelope function description is simple and versatile and often leads to analytical results. In Chapter 3, we give a short introduction to the nonlinear optics and present the mathematical description of the nonlinear susceptibilities with their brief mathematical derivations. The Pöschl-Teller potential with its mathematical properties is discussed in Chapter 4. Solutions to the Pöschl-Teller potential are given explicitly. The wave functions and the corresponding energy levels of the Pöschl-Teller potential

under a static electric field are calculated by the variational methods. We calculate the second-order nonlinearities, such as second-harmonic generation and the optical rectification of quantum well described by a Pöschl-Teller potential in Chapter 5. The results are discussed. The third-order nonlinearities, such as nonlinear absorption coefficient, intensity-dependent refractive index and third-harmonic generation, are studied and the results are discussed in Chapter 6. We calculate the nonlinear absorption coefficient in a Si- δ -doped quantum well, including the effects of the Coulomb interaction, in Chapter 7. Finally, we make a brief conclusion concerning our results in Chapter 8.

CHAPTER 2

SEMICONDUCTOR QUANTUM WELLS

2.1 Introduction

In this chapter, we discuss the general properties of the semiconductor heterostructures and of the growth techniques in brief. We introduce the envelope function description of the eigenstates of a carrier, such as an electron and a hole, trapped in a potential well formed by semiconductor heterostructures. As a specific example, wave functions and the corresponding energy levels of a finite square quantum well are obtained within the envelope function description.

2.2 General Properties of Heterostructures

A semiconductor heterostructure constitutes more than one type of semiconductor. A well-known example is GaAs/Al_xGa_{1-x}As. A perfect heterostructure requires that the constituting semiconductors must have the same crystal structure (or at least symmetry) and two lattice constants must be nearly identical [15].

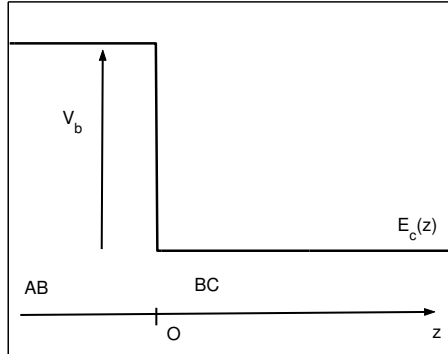


Figure 2.1: Schematic view of a heterostructure formed by two perfectly lattice-matched semiconductors, A and B whose chemical formulae are CB and AB, respectively. $E_c(z)$ stands for the position-dependent conduction band edge.

A schematic representation of an ideal interface is shown in Fig.(2.1). Note that there is a potential barrier V_b created due to the difference between the bandgaps of the semiconductors AB and CB. A quantum well is created when another layer of semiconductor AB is grown at the other side of the heterostructure, so that an electron feels a one-electron potential between the layers A-B.

In Fig.(2.2), the lattice constants and the minimum band gap of several semiconductors are shown. The figure explains the popularity of the GaAs/ $\text{Al}_x\text{Ga}_{1-x}\text{As}$: the lattice constant changes by less than 0.15% as a function of x , allowing the growth of GaAs and AlAs or $\text{Al}_x\text{Ga}_{1-x}\text{As}$ on top of one another without significant stress. Other, almost perfectly matched-alloys, are $\text{Ga}_{0.47}\text{In}_{0.53}\text{As}/\text{InP}$ and $\text{Al}_{0.48}\text{In}_{0.52}\text{As}/\text{InP}$ [16, 17].

Depending on the conduction and valence band edges, two types of quantum

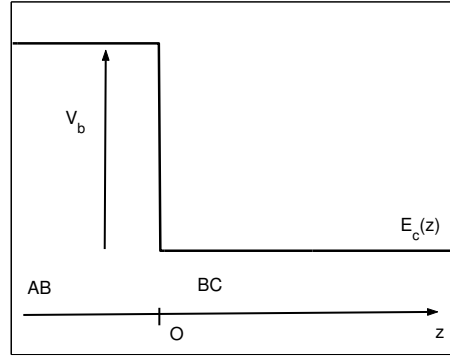


Figure 2.2: The various semiconductors plotted as a function of lattice constant and energy gap. the full lines indicate a direct-gap semiconductor and the broken lines indicate an indirect-gap semiconductor, while the two curves related to Si refer to bulk unstrained material and the strained layer epitaxial (SLE) material.

wells are possible. In the type I quantum wells, B is a barrier for both the conduction and valence band electrons, while in the type II quantum wells, A and B acts differently for the conduction and valence band electrons, for example, if A is a well for the conduction electrons, it serves as barrier for the valence electrons (see Fig.(2.3)). GaAs/ $\text{Al}_x\text{Ga}_{1-x}\text{As}$, $\text{Ga}_{0.47}\text{In}_{0.53}\text{As}/\text{InP}$ and GaSb/AlSb constitute type I quantum well while InAs/GaSb constitute type II quantum well[15].

The heterostructures are fabricated mainly by two methods: molecular-beam epitaxy (MBE) and metal-organic chemical vapor deposition (MOCVD). A simple scheme is drawn in Fig.(2.4) to describe MBE . The main idea behind the MBE is to make the materials grow on a substrate sitting on a heated holder in an

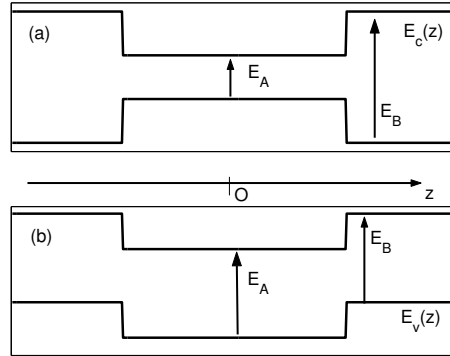


Figure 2.3: Conduction and valence band edges (a) in a type I quantum well (b) in a type II quantum wells.

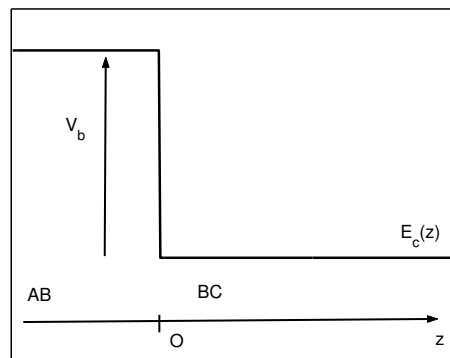
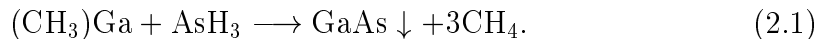


Figure 2.4: A schematic diagram of the growth chamber of an MBE machine.

evaporator that is evacuated to an ultrahigh vacuum, typically of 5×10^{-11} mbar or better by ejecting materials in vapor form from furnaces called Knudsen cells shielded by shutters. Flux of each element is controlled by the temperature of each furnace. MBE is advantageous in that it allows to grow highly abrupt junctions between different materials, gives good control of the thickness of layers, and has reasonable reproducibility. However, some disadvantages are its cost and the limited scalability of the process for production [16, 17].

MOCVD is simply described in Fig.(2.5). The substrate is placed on a heated holder in a chamber through which different gases are passed in a carrier of hydrogen. The composition of the gases are varied rapidly to control the composition of the material grown. The basic chemical reaction for growing GaAs is



The main advantages of MOCVD are that the process is faster and it has been successfully scaled up for commercial production. Regrowth, subsequent usage of the substrate for further growth, is successful. However, contamination by carbon and some serious safety problems arise with MOCVD [16, 17].

2.3 Envelope Function Description

The optical properties of semiconductor heterostructures can be understood once the electronic band structure, including the energy levels and the corresponding wave functions, are known. There are several ways to calculate the

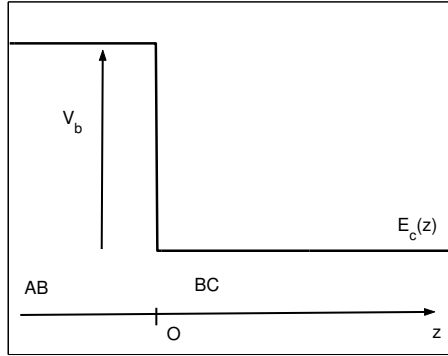


Figure 2.5: A schematic diagram of the growth cell of an MOCVD reactor.

electronic structure, such as envelope function description, tight-binding calculations and the pseudo-potential formalism [15]. We concentrate on the envelope function description to describe the electronic structure of a given semiconductor heterostructure in this section.

Envelope function description of eigenstates in a heterostructure is a simple one based on the Kane analysis of the dispersion relations of the host materials. The main goal of the description is to find the boundary conditions fulfilled by the slowly varying part of the heterostructure wave functions at interfaces. Although this model is simple and versatile and often leads to analytical results, it is valid only in the vicinity of the high-symmetry points in the host's Brillouin zone (Γ , X, L). Other approximations, however, like empirical tight-binding calculations and the pseudo-potential formalism, have capacity to handle any heterostructure energy levels, like those close or far from the Γ edge. Whereas, most of the heterostructures' energy levels associated with the device applications are

closely relevant to the high symmetry points in the host Brillouin zone for which the envelope function description proved to be adequate [15].

Consider a heterostructure formed by two different semiconductors A and B whose lattice constants are assumed to be identical and which crystallize with the same crystallographic structure. These conditions quite well satisfied by GaAs-Ga(Al)As and Ga_{0.47}In_{0.53}As-InP Under flat band-conditions, that is in case of no charge carriers, we assume that the following are held [15]:

i) The wave functions, $\psi(\mathbf{r})$, inside each layer of the heterostructure are expanded in terms of the periodic parts of the Bloch functions of the band edges under consideration

$$\psi(\mathbf{r}) = \sum_j g_j^{(A)}(\mathbf{r}) u_{j,\mathbf{k}_0}^{(A)}(\mathbf{r}) \quad (2.2)$$

and

$$\psi(\mathbf{r}) = \sum_j g_j^{(B)}(\mathbf{r}) u_{j,\mathbf{k}_0}^{(B)}(\mathbf{r}) \quad (2.3)$$

where \mathbf{r} in Eq. (2.2) and Eq. (2.3) corresponds to layer A and B , respectively. In equations above, \mathbf{k}_0 is the point in the Brillouin zone around which the heterostructure states are built and the summation over j runs over as many edges as included in the analysis.

ii) The periodic parts of the Bloch functions are assumed to be the same in each kind of layer constituting the heterostructure:

$$u_{j,\mathbf{k}_0}^{(A)}(\mathbf{r}) = u_{j,\mathbf{k}_0}^{(B)}(\mathbf{r}), \quad (2.4)$$

leading to the following simplification in the wave function

$$\psi(\mathbf{r}) = \sum_j g_j^{(A,B)}(\mathbf{r}) u_{j,\mathbf{k}_0}(\mathbf{r}). \quad (2.5)$$

Consequently, our task reduces to find out the slowly varying envelope functions $g_j^{(A,B)}(\mathbf{r})$.

The envelope function approach has been proved fruitful when applied to the problems concerning the Γ -related states of a variety of III-V heterostructures, such as GaAs-Ga(Al)As, Ga_{0.47}In_{0.53}As–InP and GaSb-InAs [15]. Therefore, the following mathematical derivations will be restricted to the Γ -related extrema, $\mathbf{k}_0 = \mathbf{0}$.

Assuming that the growth axis is $\hat{\mathbf{z}}$ axis, let the plane $z = z_0$ be the interface separating the A and B layers. Then

$$g_j^{(A)}(\mathbf{r}_\perp, z_0) = g_j^{(B)}(\mathbf{r}_\perp, z_0), \quad (2.6)$$

as the $u_{j,0}$ are linearly independent and as $\psi(\mathbf{r})$ has to be continuous at $z = z_0$. In the equation above, \mathbf{r}_\perp stands for the two-dimensional position vector. Because the lattice constants of the constituting layers are identical or almost the same, the heterostructure is translationally invariant in the layer plane. That symmetry in the layer plane makes the g_j divide into the following parts in each layer,

$$g_j^{(A,B)}(\mathbf{r}_\perp, z_0) = \frac{1}{\sqrt{S}} \exp(i \mathbf{k}_\perp \cdot \mathbf{r}_\perp) \chi_j^{(A,B)}(z), \quad (2.7)$$

where S is the sample area and $\mathbf{k}_\perp = (k_x, k_y)$ is a two-dimensional wave vector same in the layers A and B to satisfy the translational invariance. $\chi_j^{A,B}(z)$ are

the slowly varying functions of z at the scale of the hosts' unit cell in the equation above[15].

In conclusion, our wave function $\phi(\mathbf{r})$ is a sum of the products of two different set of functions:

- i) $u_{j,\mathbf{0}}$'s are rapidly varying functions, periodic with the hosts' periodicity,
- ii) g_j 's are slowly varying *envelope functions*.

Let H be the Hamiltonian describing the motion of a charge carrier in the heterostructure, that is

$$H = \frac{p^2}{2m_0} + V_A(\mathbf{r})\Theta_A + V_B(\mathbf{r})\Theta_B \quad (2.8)$$

where Θ_X is the step function giving unity if \mathbf{r} corresponds to the layer X . H , acting upon $\psi(\mathbf{r})$, gives the following eigenvalue equation satisfied by $\chi_j^{A,B}$:

$$\Xi^0(z, -i\hbar \frac{\partial}{\partial z})\chi = \epsilon\chi \quad (2.9)$$

where χ is a N -dimensional column vector and Ξ^0 a $N \times N$ matrix in which N is the number of band edges. The elements of matrix Ξ are

$$\begin{aligned} \Xi_{nm}^0(z, \frac{\partial}{\partial z}) = & \left[\epsilon_{n,0}^{(A)}\Theta_A + \epsilon_{n,0}^{(B)}\Theta_B + \frac{\hbar^2 k_{\perp}^2}{2m_0} - \frac{\hbar^2}{2m_0} \frac{\partial^2}{\partial z^2} \right] \delta_{n,m} + \\ & \frac{\hbar \mathbf{k}_{\perp}}{m_0} \cdot \langle n | \mathbf{p}_{\perp} | m \rangle - \frac{i\hbar}{m_0} \langle n | p_z | m \rangle \frac{\partial}{\partial z}, \end{aligned} \quad (2.10)$$

where $\epsilon_{n,0}^{(A,B)}$ are the energies of the n^{th} band edge at the zone center of the layers A and B, respectively and

$$\langle n | \mathbf{p} | m \rangle = \int_{\Omega} u_{n,\mathbf{0}\mathbf{P}}^* u_{m,\mathbf{0}\mathbf{P}} \mathbf{dr}. \quad (2.11)$$

A detailed mathematical derivation of Eq. (2.10) is given by Bastard [15]. In Eq. (2.10), a practical definition like $V_n(z) = 0$ if z correspond to the layer A and $V_n(z) = \epsilon_{n,0}^B - \epsilon_{n,0}^A$ if z correspond to the layer B can be made [15].

The accuracy of the results of Eq. (2.10) depend on the number N if the valence bands are needed. However, the bands Γ_6 , Γ_7 and Γ_8 , making $N=8$, will be good enough to produce highly accurate results. The influence of the other host's bands far from the Γ_6 , Γ_7 and Γ_8 edges can be treated perturbatively. Keeping terms up to the second-order in \mathbf{p} , the matrix Ξ^0 is replaced with

$$\Xi = \Xi^0 - \frac{\hbar^2}{2} \sum_{\alpha,\beta} \frac{\partial}{\partial r_\alpha} \frac{1}{\underline{M}^{\alpha\beta}} \frac{\partial}{\partial r_\beta}, \quad \alpha, \beta = x, y, z, \quad (2.12)$$

where $\underline{M}^{\alpha\beta}$ is 8×8 matrix whose elements are given by

$$\frac{m_0}{\underline{M}_{nm}^{\alpha\beta}} = \frac{2}{m_0} \sum_{\nu} \langle n | p_\alpha | \nu \rangle \frac{1}{\bar{\epsilon} - \epsilon_{\nu 0}^{(A)} - V_\nu(z)} \langle \nu | p_\beta | m \rangle, \quad (2.13)$$

where ν denotes the remote Γ edges of the host layers and $\bar{\epsilon}$ is an average energy of the Γ_6 , Γ_7 and Γ_8 set in the heterostructure [15].

Eq. (2.12) is a set of second-order differential equations whose solution provide us with the slowly varying heterostructure eigenfunctions and energy levels. Note that microscopic details of the heterostructures are not presented explicitly, instead they appear implicitly through effective parameters: the interband matrix elements $\langle n | \mathbf{p} | m \rangle$, the effective mass tensor $\underline{M}_{nm}^{\alpha\beta}$ and the band offsets V_n [15].

The boundary conditions which have to satisfied by the envelope function, χ ,

are

$$\chi^{(A)}(z = z_0) = \chi^{(B)}(z = z_0) \quad (2.14)$$

and

$$\Lambda^{(A)}\chi^{(A)}(z = z_0) = \Lambda^{(B)}\chi^{(B)}(z = z_0) \quad (2.15)$$

where Λ is a 8×8 matrix whose elements are, at most, of the first order in $\frac{\partial}{\partial z}$:

$$\Lambda_{nm} = -\frac{\hbar^2}{2m_0} \left[\left(\delta_{nm} + \frac{m_0}{\underline{M}_n^{zz}} \right) \frac{\partial}{\partial z} + \frac{2i}{\hbar} \langle n | p_z | m \rangle + i \sum_{\alpha=x,y} \frac{m_0}{\underline{M}_{nm}^{z\alpha}} k_\alpha \right], \quad (2.16)$$

with the property, $\underline{M}_{nm}^{zz} = \underline{M}_n^{zz} \delta_{nm}$. Note that the well-known boundary condition, that is the continuity of $\frac{d\chi}{dz}$ across the interface, is only a very special case of Eq. (2.16)[15].

A practical and a simple model to find out the energy levels in a heterostructure is the Ben Daniel-Duke model [15]. The basic idea behind the model is the construction of envelope function from host quantum states belonging to a single parabolic band. This is good if we can neglect the influence of the valence bands. This approximation gives the lowest conduction states of GaAs-Ga(Al)As heterostructures with GaAs layer thickness larger $\sim 100 \text{ \AA}$. For nearly isotropic conduction band, far from all the host bands, Eq. (2.12) reads

$$\left[\epsilon_s + V_b - \frac{\hbar^2}{2} \frac{\partial}{\partial z} \frac{1}{\mu(z)} \frac{\partial}{\partial z} + \frac{\hbar^2 k_\perp^2}{2\mu(z)} \right] \chi(z) = E\chi(z) \quad (2.17)$$

where V_b is energy shift of the conduction band edge when moving from the layer A to B, and $\mu(z)$ is the effective mass which is $m_{A(B)}$ when the layer A(B) is

considered. Under these circumstances, the boundary conditions obeyed by $\chi(z)$ is that

$$\chi(z) \text{ and } \frac{1}{\mu(z)} \frac{d\chi}{dz} \quad (2.18)$$

are both continuous across the interfaces A-B. An interesting feature of the effective mass mismatch across the interfaces is that it contributes to the total confining barrier by an amount depending on k_{\perp} . It also makes the derivative of the envelope function discontinuous at the interfaces [15].

To illustrate this point, let's consider a GaAs/Al_xGa_{1-x}As (for $x < 0.4$) quantum well having well width of L_W . The band offset, or the barrier height, is taken to be V_B while the effective masses in the well and the barriers are m_W and m_B . Then the effective barrier height, $V_b + \hbar^2 k_{\perp}^2 / 2\mu(z)$, in Eq. (2.17), becomes symmetric with respect to the middle of the well. For such a system, the solution of Eq. (2.17) with the boundary conditions in Eq. (2.18) yield [18]

$$\phi_1(z) = N_1 \begin{cases} \exp[\kappa_1(z + L_W/2)] \cos(k_1 L_W/2) & \text{if } z < -L_W/2 \\ \cos k_1 z & \text{if } z < |L_W/2| \\ \exp[-\kappa_1(z - L_W/2)] \cos(k_1 L_W/2) & \text{if } z > L_W/2 \end{cases} \quad (2.19)$$

with

$$N_1 = [L_W/2 + (V_B/\kappa_1 E_1) \cos^2(k_1 L_W/2)]^{-1/2} \quad (2.20)$$

and

$$\phi_2(z) = N_2 \begin{cases} -\exp[\kappa_2(z + L_W/2)] \sin(k_2 L_W/2) & \text{if } z < -L_W/2 \\ \sin k_2 z & \text{if } z < |L_W/2| \\ \exp[-\kappa_2(z - L_W/2)] \sin(k_2 L_W/2) & \text{if } z > L_W/2 \end{cases} \quad (2.21)$$

with

$$N_2 = [L_W/2 + (V_B/\kappa_2 E_2) \sin^2(k_2 L_W/2)]^{-1/2} \quad (2.22)$$

for the ground and first excited states, respectively. In equations above, $k_{1,2} = \sqrt{2m_W E_{1,2}}/\hbar$ and $\kappa_{1,2} = \sqrt{2m_B(V_B - E_{1,2})}/\hbar$ where E_1 and E_2 are the ground and first excited state eigenenergies determined by the roots of the following equations

$$\cos(k_1 L_W/2) - \frac{m_B k_1}{m_W \kappa_1} \sin(k_1 L_W/2) = 0, \quad (2.23)$$

and

$$\cos(k_2 L_W/2) + \frac{m_W \kappa_2}{m_B k_2} \sin(k_2 L_W/2) = 0, \quad (2.24)$$

resulting from the application of the boundary conditions (Eq. (2.18)) at the interfaces, $z = \pm L_W/2$, respectively.

We have ignored the term, $\hbar^2 k_{\perp}^2/2\mu(z)$, in the calculations above since this term is very small in most cases, as in GaAs/AlGaAs heterostructures [15].

Semiconductor heterostructures are doped to form two-dimensional electron gas in the quantum well, leading to the non-flat band conditions. The doping of the heterostructure is achieved either by placing impurities directly in the well or

in the barriers. The latter has an advantage that the positive and negative charges are spatially separated, considerably lowering the impurity scattering. The basic application of the doped heterostructures is field-effect transistors, such as modulation-doped field-effect transistors (MODFET) and high electron mobility transistors (HEMT). The almost perfect crystalline quality of III-V heterostructures and the ability of the separation of carriers from the impurities create huge electron mobilities making the field-effect transistors based on the modulation-doping so popular in recent years [19, 20].

The single-particle Hamiltonian is not adequate when quantum wells are doped to supply extra electrons. The interaction between the impurities and the electrons and the interaction among the electrons themselves must be considered. Let $U^{imp}(\mathbf{r})$ be the electrostatic potential due to the impurities (which in turn defines the interaction between the electrons and the impurities) and let U^{el} be the electrostatic potential due to the interaction of the electrons themselves. If a single electron is considered, the expression

$$U^{el} = -e \int d\mathbf{r}' \rho(\mathbf{r}') \frac{1}{|\mathbf{r} - \mathbf{r}'|} \quad (2.25)$$

defines the electrostatic potential due to the electric field of the remaining electrons (they are treated as a smooth distribution of negative charge). The charge density $\rho(\mathbf{r})$, defining this charge distribution, is given by

$$\rho(\mathbf{r}) = -e \sum_i |\psi_i(\mathbf{r})|^2, \quad (2.26)$$

where all occupied one-electron levels are considered [21].

The N -particle Hamiltonian is obtained by inserting the expressions for U^{imp} and U^{el} and the result is known as Hartree equations. They give the best approximation to the full N -electron wave function,

$$\Psi(\mathbf{r}_1\mathbf{s}_1, \mathbf{r}_2\mathbf{s}_2, \dots, \mathbf{r}_N\mathbf{s}_N) = \psi_1(\mathbf{r}_1\mathbf{s}_1)\psi_2(\mathbf{r}_2\mathbf{s}_2) \dots \psi_N(\mathbf{r}_N\mathbf{s}_N), \quad (2.27)$$

where ψ_i are a set of N orthonormal one-electron wave functions. However, Eq. (2.27) does not satisfy the Pauli exclusion principle. It should be an antisymmetric wave function. Instead, if we rewrite it as

$$\Psi(\mathbf{r}_1\mathbf{s}_1, \mathbf{r}_2\mathbf{s}_2, \dots, \mathbf{r}_N\mathbf{s}_N) = \frac{1}{\sqrt{N!}} \begin{vmatrix} \psi_1(\mathbf{r}_1\mathbf{s}_1)\psi_1(\mathbf{r}_2\mathbf{s}_2) \dots \psi_1(\mathbf{r}_N\mathbf{s}_N) \\ \psi_2(\mathbf{r}_1\mathbf{s}_1)\psi_2(\mathbf{r}_2\mathbf{s}_2) \dots \psi_2(\mathbf{r}_N\mathbf{s}_N) \\ \cdot & \cdot & \cdot \\ \cdot & \cdot & \cdot \\ \cdot & \cdot & \cdot \\ \psi_N(\mathbf{r}_1\mathbf{s}_1)\psi_N(\mathbf{r}_2\mathbf{s}_2) \dots \psi_N(\mathbf{r}_N\mathbf{s}_N) \end{vmatrix} \quad (2.28)$$

we obtain an antisymmetric wave function, satisfying the Pauli exclusion principle. Inserting, Eq. (2.28) into the N -particle Hamiltonian with U^{imp} and U^{el} , we get the following

$$\begin{aligned} \langle H \rangle_{\Psi} &= \sum_i \int d\mathbf{r} \psi_i^* \mathbf{r} \left(-\frac{\hbar^2}{2m} \nabla^2 + U^{imp}(\mathbf{r}) \right) \psi_i(\mathbf{r}) \\ &+ \frac{1}{2} \sum_{i,j} \int d\mathbf{r} d\mathbf{r}' \frac{e^2}{|\mathbf{r} - \mathbf{r}'|} |\psi_i(\mathbf{r})|^2 |\psi_j(\mathbf{r}')|^2 \\ &- \frac{1}{2} \sum_{i,j} \int d\mathbf{r} d\mathbf{r}' \frac{e^2}{|\mathbf{r} - \mathbf{r}'|} \delta_{s_i s_j} \psi_i^*(\mathbf{r}) \psi_i(\mathbf{r}') \psi_j^*(\mathbf{r}) \psi_j(\mathbf{r}'). \end{aligned} \quad (2.29)$$

The last term in Eq. (2.29) is additional and different than the U^{el} . It is called the exchange term, and the Hamiltonian including this term is called Hartree-Fock Hamiltonian. The correction to this approximation is referred to as the correlation term [21].

We calculate the optical properties of δ -doped quantum wells in Chapter 7. In these systems, where very high density of electrons are encountered, like 10^{12} cm^{-2} , the exchange and correlation terms are negligible [22] whereas the Hartree term makes the major contribution to the confining potential. We have included the exchange and correlation effects and found the results to be unaffected. Therefore, we ignore exchange and correlation terms in our calculations.

The envelope function scheme described in this chapter will be used to calculate the energy eigenstates of the carriers trapped in the potential created by the heterostructures. Our next task is to apply the idea discussed above to find out the nonlinear optical properties in a model quantum well which is the subject of the following chapters.

CHAPTER 3

NONLINEAR OPTICS

3.1 Introduction

This chapter deals with the quantum-mechanical treatment of the nonlinear susceptibilities. The nonlinear susceptibilities are derived using the laws of quantum mechanics. This involves a perturbational solution to the density matrix equation. Second- and third-order susceptibilities are obtained for general n -level quantum mechanical system. The results are presented in a very compact form.

3.2 A Simple Description

It is called nonlinear optics because the response of the material to an applied optical field depends in a nonlinear way upon the strength of the optical field. We can explain more concretely that nonlinearity by expanding the polarization of the material, which is defined as the dipole moment per volume, in powers of

the strength of the applied optical field, $\mathbf{E}(t)$:

$$\mathbf{P}(t) = \chi^{(1)}\mathbf{E}(t) + \chi^{(2)}\mathbf{E}^2(t) + \chi^{(3)}\mathbf{E}^3(t) + \dots, \quad (3.1)$$

where $\chi^{(1)}$, $\chi^{(2)}$ and $\chi^{(3)}$ are linear, second-order and third-order susceptibilities, respectively. When we write Eq. (3.1) it is assumed that the polarization at time t depends only on the instantaneous value of the electric field strength. The susceptibilities are tensors of several ranks. The even powers of susceptibilities are nonzero only in noncentrosymmetric materials, that is, in materials that do not show inversion symmetry. The typical values of $\chi^{(2)}$ and $\chi^{(3)}$ for condensed matter, under the nonresonant condition, are 5×10^{-8} and 3×10^{-15} esu, respectively [23, 24, 25].

The consequences of Eq. (3.1) can become more concrete through a simple example. Consider a monochromatic applied field in one dimension, such that

$$E(t) = E \cos \omega t. \quad (3.2)$$

The application of Eq. (3.2) to Eq. (3.1) yield the following results:

$$P(t) = \frac{1}{2}\chi^{(2)}E^2 + \left(\chi^{(1)}E + \frac{3}{4}\chi^{(3)}E^3\right) \cos \omega t + \frac{1}{2}\chi^{(2)}E^2 \cos 2\omega t + \frac{1}{4}\chi^{(3)}E^3 \cos 3\omega t \quad (3.3)$$

using relevant trigonometric identities. The first term in Eq. (3.3), independent of the frequency, creates a static electric field within the material. This process is called optical rectification. The second term in the parenthesis is the

nonlinear contribution of the polarization at the frequency of the applied field. That term creates a nonlinear contribution to the refractive index. The third term in Eq. (3.3) implies a generation of radiation at the frequency twice that of the applied field which is called second-harmonic generation. The last term Eq. (3.3) describes a radiation having a frequency three times larger than that of the applied field. This process is called third-harmonic generation [24, 23, 25].

3.3 Quantum-Mechanical Theory of Nonlinear Susceptibilities

Nonlinear optical susceptibilities are characteristic properties of a material. The electronic and molecular structure of the material determine the nonlinear optical susceptibilities. Their microscopic expressions can be derived using the laws of quantum mechanics, allowing us to understand how the susceptibilities depend upon the dipole moments, atomic energy levels and the other material parameters. Besides, the expressions will show the internal symmetries of the susceptibilities and will help us to obtain predictions of their numerical values.

The density matrix formulation of the quantum mechanics is the best way to calculate nonlinear susceptibilities when the relaxation of excitations are included.

The density matrix operator satisfies the following equation of motion

$$\frac{\partial \rho}{\partial t} = \frac{1}{i\hbar} [H_0 + H_{int}, \rho], \quad (3.4)$$

also known as the Liouville equation. Here H_0 is the unperturbed Hamiltonian and H_{int} is the interaction Hamiltonian of the material with the applied optical

field. While Eq. (3.4) describes the time evolution of the density matrix operator, we should include the random perturbations on our system by the thermal reservoir around it. Let H_{rand} be the Hamiltonian describing such perturbations. Since H_{rand} will be responsible for relaxations of the excitations, that is the relaxation of the perturbed ρ back to the thermal equilibrium, we may write

$$\left(\frac{\partial \rho}{\partial t}\right)_{relax} = \frac{1}{i\hbar} [H_{rand}, \rho]. \quad (3.5)$$

Let $|n\rangle$ be the eigenstates of the Hamiltonian H_0 and let $\rho_{nm} = \langle n|\rho|m\rangle$. ρ_{nm} relaxes to its equilibrium value $\rho_{nm}^{(eq)}$ at thermal equilibrium. We assume that $\rho_{nm}^{(eq)} = 0$ for $n \neq m$. This is physical because thermal excitation, which is expected to be a random process, can not produce any coherent admixture of the states, $|n\rangle$ and $|m\rangle$. Then we write Eq. (3.5) as

$$\left(\frac{\partial \rho_{nm}}{\partial t}\right)_{relax} = -\Gamma_{nm}(\rho_{nm} - \rho_{nm}^{(eq)}) \quad (3.6)$$

where Γ_{nm} is the decay rate between the states $|n\rangle$ and $|m\rangle$ and we assume that Γ_{nm} is real which leads to $\Gamma_{nm} = \Gamma_{mn}$. Adding Eq. (3.6) to Eq. (3.4), we obtain the final form

$$\frac{\partial \rho_{nm}}{\partial t} = \frac{1}{i\hbar} [H_0 + H_{int}, \rho]_{nm} - \Gamma_{nm}(\rho_{nm} - \rho_{nm}^{(eq)}). \quad (3.7)$$

for the time evaluation equation of matrix elements of the density matrix.

3.4 Perturbation Solution of the Density Matrix Equation

A fully analytical solution of Eq. (3.7) is not available for the physical systems of interest. However, a perturbative solution can be adapted. The expectation value and the matrix elements of the interaction Hamiltonian H_{int} are assumed to be much smaller than the expectation value of H_0 which means a weak interaction. We assume that the interaction of the material with the applied optical field is described sufficiently well by the electric dipole approximation as

$$H_{int} = -\boldsymbol{\mu} \cdot \mathbf{E}(t), \quad (3.8)$$

where $\nu = -e\mathbf{r}$ stands for the electric dipole moment operator.

Eq. (3.7) can be rewritten as follows

$$\frac{\partial \rho_{nm}}{\partial t} = -i\omega_{nm}\rho_{nm} + \frac{1}{i\hbar} \sum_k \{ (H_{int})_{nk}\rho_{km} - \rho_{nk}(H_{int})_{km} \} - \Gamma_{nm}(\rho_{nm} - \rho_{nm}^{(eq)}) \quad (3.9)$$

using the base vectors, $|n\rangle$. Our perturbative approach dictates the replacement of each $(H_{int})_{ij}$ in Eq. (3.9) by $\lambda(H_{int})_{ij}$. By such a replacement, we aim to control the strength of the perturbation by λ ranging from 0 to 1. Our next task is to investigate a solution to Eq. (3.9) in the form a power series in λ that can be stated as

$$\rho_{nm} = \rho_{nm}^{(0)} + \lambda\rho_{nm}^{(1)} + \lambda^2\rho_{nm}^{(2)} + \dots \quad (3.10)$$

Then, the coefficients of each power of λ must satisfy the Eq. (3.9) separately,

leading to the following set of equations

$$\frac{\partial \rho_{nm}^{(0)}}{\partial t} = -i\omega_{nm}\rho^{(0)} - \Gamma_{nm}(\rho_{nm}^{(0)} - \rho_{nm}^{(eq)}), \quad (3.11)$$

$$\frac{\partial \rho_{nm}^{(1)}}{\partial t} = -(i\omega_{nm} + \Gamma_{nm})\rho_{nm}^{(1)} + \frac{1}{i\hbar} [H_{int}, \rho^{(0)}]_{nm}, \quad (3.12)$$

$$\frac{\partial \rho_{nm}^{(2)}}{\partial t} = -(i\omega_{nm} + \Gamma_{nm})\rho_{nm}^{(2)} + \frac{1}{i\hbar} [H_{int}, \rho^{(1)}]_{nm}, \quad (3.13)$$

and so on. The set of equations above are coupled linear differential equations, once $\rho_{nm}^{(0)}$ is known, the higher orders of $\rho_{nm}^{(k)}$ are obtained by integrating the equations in order. The steady-state solution to Eq. (3.11) is taken to be as

$$\rho_{nm}^{(0)} = \rho_{nm}^{(eq)} \quad (3.14)$$

(note that Eq. (3.11) does not include any interaction term related with the applied field). Integration of Eq. (3.12) will give us

$$\rho_{nm}^{(1)} = \int_{-\infty}^t \frac{1}{i\hbar} [H_{int}(t'), \rho^{(0)}]_{nm} \exp\{(i\omega_{nm} + \Gamma_{nm})(t' - t)\} dt' \quad (3.15)$$

The next order of $\rho_{nm}^{(n)}$ can be easily obtained in the same manner.

Let the applied optical field be represented as

$$\mathbf{E}(t) = \sum_s \mathbf{E}_s \exp(-i\omega_s t). \quad (3.16)$$

Then, using Eq. (3.8), Eq. (3.15) and Eq. (3.16), we obtain the following expression for the $\rho_{nm}^{(1)}$

$$\rho_{nm}^{(1)}(t) = (\rho_{mm}^{(0)} - \rho_{nn}^{(0)}) \sum_s \frac{\mu_{nm} \cdot \mathbf{E}_s \exp(-i\omega_s t)}{\hbar [\omega_{nm} - \omega_s - i\Gamma_{nm}]} \quad (3.17)$$

It is straightforward to obtain the expression for $\rho_{nm}^{(2)}$ by using Eq. (3.17). But the result is quite lengthy to present.

We can make a power series expansion of the polarization

$$\mathbf{P} = \lambda \mathbf{P}^{(1)} + \lambda^2 \mathbf{P}^{(2)} + \dots \quad (3.18)$$

like ρ_{nm} . As we know from quantum mechanics, expectation value of an observable is given as $\mathbf{A} = \text{Tr}(\rho \mathbf{A})$. Since $\mathbf{P} = N \langle \mu \rangle$ where N is the atomic number density, we have

$$\mathbf{P}^{(1)} = N \text{Tr}(\rho^{(1)} \mu). \quad (3.19)$$

Therefore, if we take the trace in Eq. (3.19) and use the relation $\mathbf{P}^{(1)} = \chi^{(1)} \mathbf{E}$ we obtain the following expression for the linear susceptibility

$$\chi^{(1)}(\omega_s) = N \sum_{nm} (\rho_{mm}^{(0)} - \rho_{nn}^{(0)}) \frac{\mu_{mn} \mu_{nm}}{\hbar [\omega_{nm} - \omega_s - i\Gamma_{nm}]} \quad (3.20)$$

Similarly, the second-order and third-order nonlinear susceptibilities can be obtained easily. The results are

$$\begin{aligned} \chi_{ijk}^{(2)}(\omega_s + \omega_r, \omega_s, \omega_r) = & \frac{N}{2\hbar^2} \sum_{m\nu\nu} (\rho_{mm}^{(0)} - \rho_{\nu\nu}^{(0)}) \\ \times \left\{ & \frac{\mu_{mn}^i \mu_{n\nu}^j \mu_{\nu m}^k}{[\omega_{nm} - \omega_s - \omega_r - i\Gamma_{nm}] [\omega_{\nu m} - \omega_r - i\Gamma_{\nu m}]} \right. \\ & + \frac{\mu_{mn}^i \mu_{n\nu}^k \mu_{\nu m}^j}{[\omega_{nm} - \omega_s - \omega_r - i\Gamma_{nm}] [\omega_{\nu m} - \omega_s - i\Gamma_{\nu m}]} \\ & - \frac{\mu_{n\nu}^i \mu_{mn}^j \mu_{\nu m}^k}{[\omega_{\nu n} - \omega_s - \omega_r - i\Gamma_{\nu n}] [\omega_{\nu m} - \omega_r - i\Gamma_{\nu m}]} \\ & \left. - \frac{\mu_{n\nu}^i \mu_{mn}^k \mu_{\nu m}^j}{[\omega_{\nu n} - \omega_s - \omega_r - i\Gamma_{\nu n}] [\omega_{\nu m} - \omega_s - i\Gamma_{\nu m}]} \right\}, \quad (3.21) \end{aligned}$$

$$\begin{aligned}
\chi_{kjh}^{(3)}(\omega_q + \omega_s + \omega_r, \omega_q, \omega_s, \omega_r) &= \frac{N}{\hbar^3} P_I \sum_{nm\nu l} \\
&\left\{ \frac{(\rho_{mm}^{(0)} - \rho_{ll}^{(0)}) \mu_{mn}^k \mu_{n\nu}^j \mu_{\nu l}^i \mu_{lm}^h}{[\omega_{lm} - \omega_r - i\Gamma_{lm}] [\omega_{\nu m} - \omega_r - \omega_s - i\Gamma_{\nu m}] [\omega_{nm} - \omega_r - \omega_s - \omega_q - i\Gamma_{nm}]} \right. \\
&\quad - \frac{(\rho_{ll}^{(0)} - \rho_{\nu\nu}^{(0)}) \mu_{mn}^k \mu_{n\nu}^j \mu_{lm}^i \mu_{\nu l}^h}{[\omega_{\nu l} - \omega_r - i\Gamma_{\nu l}] [\omega_{\nu m} - \omega_r - \omega_s - i\Gamma_{\nu m}] [\omega_{nm} - \omega_r - \omega_s - \omega_q - i\Gamma_{nm}]} \\
&\quad - \frac{(\rho_{\nu\nu}^{(0)} - \rho_{ll}^{(0)}) \mu_{mn}^k \mu_{\nu m}^j \mu_{nl}^i \mu_{l\nu}^h}{[\omega_{l\nu} - \omega_r - i\Gamma_{lm}] [\omega_{n\nu} - \omega_r - \omega_s - i\Gamma_{n\nu}] [\omega_{nm} - \omega_r - \omega_s - \omega_q - i\Gamma_{nm}]} \\
&\quad \left. + \frac{(\rho_{ll}^{(0)} - \rho_{nn}^{(0)}) \mu_{mn}^k \mu_{\nu m}^j \mu_{l\nu}^i \mu_{nl}^h}{[\omega_{nl} - \omega_r - i\Gamma_{nl}] (\omega_{\nu m} - \omega_r - \omega_s - i\Gamma_{\nu m}) [\omega_{nm} - \omega_r - \omega_s - \omega_q - i\Gamma_{nm}]} \right\}, \tag{3.22}
\end{aligned}$$

respectively. Here $\mathcal{P}_{\mathcal{I}}$ means that everything to the right of it is to be averaged over all possible permutations of the input frequencies ω_q , ω_s and ω_r , with the cartesian indices h, i, j permuted simultaneously.

The expressions for $\chi^{(2)}$ and $\chi^{(3)}$ can be transformed into different forms depending upon the physical system under consideration. For example, when all input frequencies differ significantly from any resonance frequency of the system, then the Γ_{ij} in the denominators of Eq. (3.21) and Eq. (3.22) can be ignored. However, in this work, we will deal with the resonance cases in which the imaginary contribution in the denominators gains indispensable importance.

We have derived the expressions for the nonlinear susceptibilities, $\chi^{(2)}$ and $\chi^{(3)}$ by solving the density matrix equation perturbatively. The resulting nonlinear susceptibility expressions, Eq. (3.21) and Eq. (3.22), are given in a very compact form for an n -level quantum mechanical system. Given the explicit expressions

of the susceptibilities, the nonlinear optical properties in a specific quantum well, like Pöschl-Teller quantum well, can be calculated in a straightforward way. In fact, this is what we will do in the following chapters.

CHAPTER 4

PÖSCHL-TELLER POTENTIAL

4.1 Introduction

In this chapter, we give the mathematical description of the Pöschl-Teller potential. Its wave functions with the corresponding energy levels are discussed briefly. The potential is investigated under a dc electric field, and the solutions to the Schrödinger equation are obtained through the perturbational and variation methods since the corresponding analytic solutions do not exist. The potential itself and the first three wave functions are displayed for several values of the potential parameters.

4.2 Pöschl-Teller Potential

The Pöschl-Teller potential is given by the following [citeposchl33,flugge71,nieto78](#)

$$V(z) = \frac{\hbar^2 \beta^2}{2m^*} \left[\frac{\kappa(\kappa - 1)}{\sin^2(\beta z)} + \frac{\eta(\eta - 1)}{\cos^2(\beta z)} \right] \quad \kappa, \eta > 1, \quad (4.1)$$

where κ, η are known as the depth parameters and β as the width parameter. Clearly, the potential is periodic and each period is separated from the next by an infinite potential barrier, allowing the related Schrödinger equation to be analytically solvable. The potential has such a nice feature that it can be easily made asymmetric by a correct choice of its parameter set: κ, η , and β . It is asymmetric about $z = \pi/4\beta$ (unless $\kappa = \eta$), and the minimum of the well is located at $z_{min} > (<)\pi/4\beta$ as $\kappa > (<)\eta$. We show the potential as a function of βz for $\kappa = 1.2, 2.0$ and 3.0 indicated by solid, dashed- and dotted-lines, respectively at $\eta = 2.0$ in Fig. (4.1). As discussed above, there is a clear asymmetry in the form of the potential at nonequal values of κ and η . Note that potential is wider for small κ and narrower for large κ .

The adjustable asymmetry property of the potential and its analytic character as the solution the corresponding Schrödinger equation will help us in the investigation of the dependence of the nonlinear optical properties on the potential well parameters, such as well asymmetry, well depth or width etc.

4.3 Schrödinger equation with Pöschl-Teller Potential

The corresponding Schrödinger equation has the following eigen functions and eigenvalues[27]

$$\phi_n(z) = C_N \sin^\kappa(\beta z) \cos^\eta(\beta z) {}_2F_1\left(-n, \kappa + \eta + n, \kappa + \frac{1}{2}; \sin^2(\beta z)\right), \quad (4.2)$$

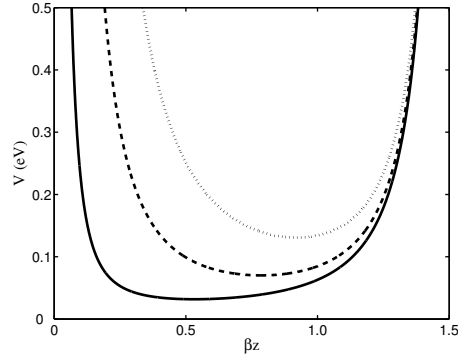
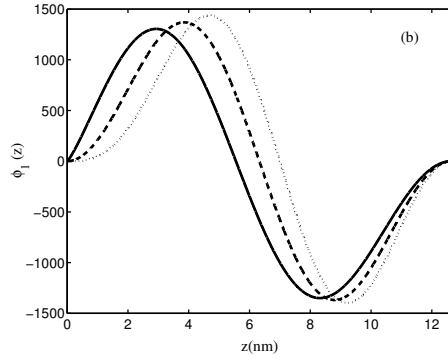
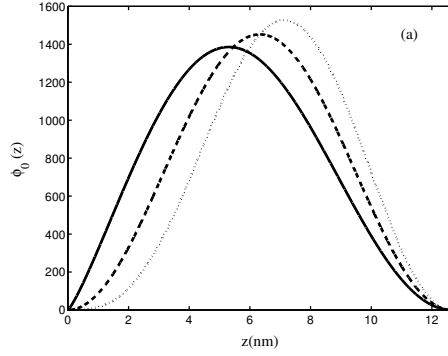


Figure 4.1: The Pöschl-Teller potential profile for $\eta = 2$. The solid, the dashed and the dotted-curves stand for $\kappa = 1.2$, $\kappa = 2$ and $\kappa = 3$, respectively.

$$E_n = \frac{\hbar^2 \beta^2}{2m^*} (\kappa + \eta + 2n)^2 \quad n = 0, 1, 2, \dots \quad (4.3)$$

Here C_N is the normalization constant and ${}_2F_1(a, b, c; f(z))$ is the Hypergeometric function. The potential has the characteristic behavior of an infinite potential, that is the energy levels are proportional to β^2 , and in turn to L^{-2} . Wave functions of the first three states are plotted in Fig. (4.2)(a)-(c). In the figures, solid, dashed- and dotted-lines stand for $\kappa = 1.2$, 2.0 and 2.8 at $\eta = 2.0$, respectively. The wave functions shift to the side where the bottom of the well sits. This is determined, as mentioned above, by the relation between κ and η . We also plot the first three energy levels as a function of κ at $\eta = 2.0$ in Fig. (4.3). As it is clear in Eq. (4.3), the energy values depend on the square of κ and the quantum



number n . We write the energy difference between two consecutive states as

$$\Delta E_{n+1,n} = \frac{2\hbar^2\beta^2}{m^*} (\kappa + \eta + 1 + 2n), \quad (4.4)$$

indicating that the energy levels are not equally spaced. The higher the quantum number, the larger the spacing.

The potential is reduced to the following form in the symmetric case (i.e. when $\kappa = \eta$)

$$V(z) = \frac{\hbar^2\beta^2}{2m^*} \frac{\kappa(\kappa - 1)}{\cos^2 \bar{z}}, \quad (4.5)$$

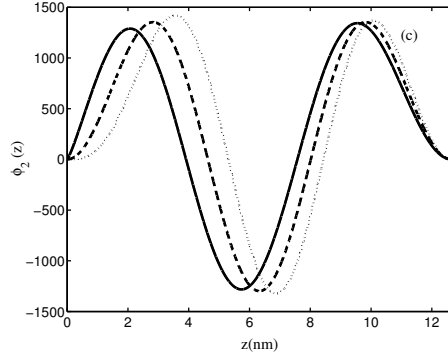


Figure 4.2: The normalized first three wave functions of a Pöschl-Teller quantum well. The solid, the dashed and the dotted-curves stand for $\kappa = 1.2$, $\kappa = 2$ and $\kappa = 3$ in panels (a), (b) and (c), respectively.

if we make a change of variables such that: $\bar{z} = 2\beta z - \pi/2$ as $\kappa \rightarrow 1$. This form of the potential gives exactly the eigenvalues and wave functions for the infinite square well potential with barriers at $\bar{z} = \pm\pi/2\beta$. Also one can show that Eq. (4.5) gives exactly the eigenvalues and the wave functions for the simple harmonic oscillator provided that the zero-point energy $\eta(\eta - 1)\hbar^2\beta^2/2m^*$ is subtracted from Eq. (4.5) and then the limits $\eta \rightarrow \infty$, $\beta \rightarrow \infty$ are taken but such that $\beta^2\eta = m^*\omega/\hbar$.

4.4 Pöschl-Teller potential under a DC electric field

The Schrödinger equation corresponding to the Pöschl-Teller potential has no analytical solutions under a static electric field applied in the z -direction. Having no analytic forms, the wave functions and eigenvalues can be calculated in several

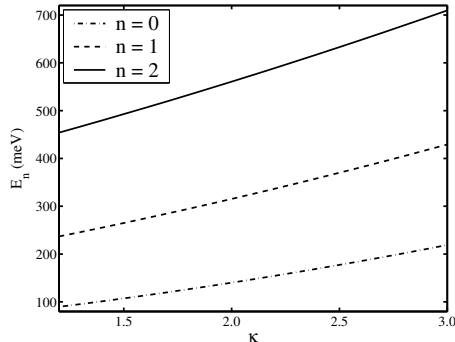


Figure 4.3: The first three energy levels of a Pöschl-Teller quantum well. The dashed-dotted-, the dashed and the solid curves stand for $n = 0$, $n = 1$ and $n = 2$, respectively.

ways, such as numerical, variational or perturbational. We use variational and perturbational methods in the calculations [29].

The variational wave functions are easy to compute and practical to follow the evolution of the physical quantities. The simple form of the trial wave function, $f_n(z) \exp(-\beta_n z)$, is proved to give accurate results for $n = 1$ for an infinite well [30], where $f_n(z)$ is the zero-field n^{th} quantum well bound state and β_n is a variational parameter. However, it provides significantly different results from the numerical calculations for the higher energy levels if these trial wave functions are not orthogonal to each other [30]. We find analytic forms of orthogonalized trial wave functions by the Gram-Schmidt orthogonalization procedure [30]. This procedure requires the construction of an orthonormal set $\{\phi_0, \phi_1, \dots\}$ from a finite or an infinite independent set $\{u_0, u_1, \dots\}$ which is not necessarily orthonormal

[30].

We suggest the following n th vector, u_n ,

$$u_n(z) = \sin^\kappa(\beta z) \cos^\eta(\beta z) {}_2F_1\left(-n, \kappa + \eta + n, \kappa + \frac{1}{2}; \sin^2(\beta z)\right) \exp\left[-\beta_n\left(\frac{z}{L} + \frac{1}{2}\right)\right] \quad (4.6)$$

which is not an orthogonal set, where β_n is the n th variational parameter. The variational wave function for the ground state is

$$\phi_0 = u_0 \langle u_0 | u_0 \rangle^{-1/2}. \quad (4.7)$$

The ground state energy is found by minimization of $E_0(\beta_0)$ with respect to β_0 .

The corresponding equation is given as

$$E_0(\beta_0) = \langle u_0 | H_z | u_0 \rangle \langle u_0 | u_0 \rangle^{-1}. \quad (4.8)$$

We start with

$$\theta = u_1 - \langle u_1 | \phi_0 \rangle \phi_0. \quad (4.9)$$

to find the first excited wave function and its energy. Here $\langle u_1 | \phi_0 \rangle$ is the inner product between the related functions. Minimization of

$$E_1(\beta_1) = \langle \theta | H_z | \theta \rangle \langle \theta | \theta \rangle^{-1} \quad (4.10)$$

with respect to β_1 provides us with the first excited state energy level. The corresponding wave function can be found as

$$\phi_1 = \theta \langle \theta | \theta \rangle^{-1/2}. \quad (4.11)$$

In Table 4.1, we show the result of the variational calculation for the first two energy levels and the transition energy from ground state to the first excited state along with the results obtained from the time-independent perturbation theory in parenthesis. Note that the results obtained using variational and perturbative techniques are very close. The transition energy E_{10} is almost constant (there is a slight blue-shift (red-shift) for small (large) κ), while the individual energies change considerably with the increasing electric field. The slight shift in the transition energy is due to the tiny change in the difference $z_{11} - z_{00}$, which is the linear term in the expression for the transition energy when the time-independent perturbation theory is used.

The modified Pöschl-Teller potential,

$$V(z) = -\frac{\hbar^2 \beta^2 \kappa (\kappa - 1)}{2m^*} \cosh^{-2}(\beta z), \quad (4.12)$$

has attracted some interest in recent years [32, 31, 33]. $V(z)$ becomes a potential barrier for $0 < \kappa < 1$, a flat band for $\kappa = 1$ and a potential well for $\kappa > 1$. Tong [32] suggested several applications in semiconductor heterojunction devices and in optical systems. Tong and Kiriushcheva [31] showed that it can be used in reduction of noise in resonance tunneling devices and other devices. Radovanovic *et al.* [33] worked out several intersubband absorption properties of the potential. An interesting point is that Eq. (4.12) for $\kappa > 1$ resembles the profile of a diffused quantum well.

In this work, we have focused on the electronic subband structure of quantum

Table 4.1: The calculated variational energy eigenvalues for the ground and first excited states and the corresponding transition energies in meV under the applied electric field for $\eta = 2$ with the results obtained through time-independent perturbation theory in parenthesis. Energies in each column represent E_0 , E_1 and E_{10} from top to bottom, respectively.

	$F = 0$ kV/cm	$F = 25$ kV/cm	$F = 50$ kV/cm	$F = 100$ kV/cm
	89.70 (89.70)	103.19 (103.20)	116.38 (116.38)	142.12 (142.01)
$\kappa = 1.2$	236.87 (236.87)	251.69 (251.69)	266.54 (266.55)	296.58 (296.64)
	147.17 (147.17)	148.50 (148.49)	150.16 (150.17)	154.46 (154.63)
	140.16 (140.16)	155.84 (155.85)	171.30 (171.31)	201.82 (201.83)
$\kappa = 2.0$	315.36 (315.36)	331.15 (331.16)	346.95 (346.96)	378.83 (378.86)
	175.12 (175.20)	175.31 (175.30)	175.65 (175.65)	177.01 (177.03)
	201.83 (201.83)	219.05 (219.06)	236.09 (236.11)	269.99 (270.04)
$\kappa = 2.8$	405.06 (405.06)	421.72 (421.73)	438.37 (438.39)	471.94 (471.97)
	203.23 (203.23)	202.67 (202.67)	202.28 (202.28)	201.95 (201.93)

wells described by Pöschl-Teller potential. The energy levels and the corresponding wave functions are given analytically as functions of the parameters of the potential. Whereas, they are calculated through variational and perturbational ways under an electric field since there is no analytic solution. The knowledge of electronic subband structure and the corresponding wave functions will help us to calculate the optical properties of Pöschl-Teller quantum wells in the following chapters.

CHAPTER 5

SECOND-ORDER NONLINEARITIES

5.1 Introduction

In this chapter we study on the second-order nonlinear optical properties in a Pöschl-Teller quantum well [69]. These include second-harmonic generation (SHG) and the optical rectification. The calculations are based on the expressions obtained through the density matrix equation in Chapter III. Only the first two levels of the quantum well is considered in numerical calculations. The effect of the DC electric field on the second-order nonlinearities are also investigated. The numerical results are discussed and compared with the results of the other quantum well systems, such as square quantum wells.

5.2 Second-Harmonic Generation

Second-order nonlinearities are nonzero only in noncentrosymmetric systems. That means a semiconductor quantum well having symmetric potential profile

will provide very small second-order nonlinearities. The asymmetric quantum wells are obtained by advanced growth techniques or applying external bias field (see Fig. (5.1)), canceling the selection rules and making nonzero second-order nonlinearities possible in semiconductor quantum wells. Since the dipole matrix elements are large in semiconductor quantum wells (typically of the same order as the size of the well) one can expect considerably large second-order nonlinearities in such systems. In fact, this was suggested by Gurnick and DeTemple [8] for an asymmetric Morse potential practically realizable in $\text{Al}_x\text{Ga}_{1-x}\text{As}$ quantum well by varying composition x in the growth direction. The resultant nonlinearities were 10-100 times larger than that in bulk crystals. The first experimental observation of second-order nonlinearities was made by Fejer *et al.* [9] in 1989. The experiment was done in a GaAs/AlGaAs quantum well by breaking the symmetry with a dc electric field of 36 kVcm^{-1} . They obtained a second-harmonic generation of 28 nm/V , which is 73 times larger than that of bulk GaAs using a $10.6 \mu\text{m}$ pump CO_2 laser. Following the work of Fejer *et al.* [9], Rosencher *et al.* [34] reported second-harmonic generation of 760 nm/V in a stepped asymmetric GaAs/AlGaAs quantum well. Boucaud *et al.* [35] measured $\chi^{(2)}$ values as much as 720 nm/V in the same structure. Sirtori *et al.* [36] measured a second-harmonic generation of 48 nm/V in an asymmetrically coupled AlGaAs/GaInAs. Later, Sirtori *et al.*[37] demonstrated Stark tuning in the same structures and they obtained a second-order susceptibility as much as 75 nm/V . By doubly-resonant difference

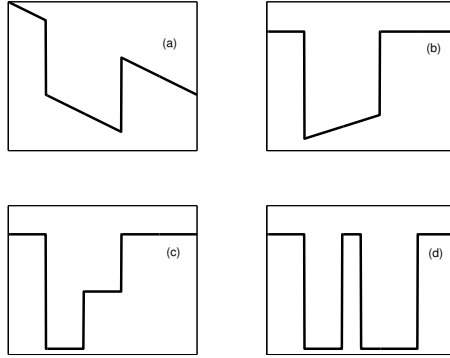


Figure 5.1: Asymmetric quantum wells. (a) Biased quantum well. (b) Graded quantum well. (c) Stepped quantum well. (d) Double quantum well.

frequency mixing of two mid infrared ($10\ \mu m$) sources, Sirtori *et al.* [38] obtained $60\ \mu m$ - radiation and a $\chi^{(2)} \cong 1000\ \text{nm/V}$.

On theoretical side, Khurgin [39, 40, 41] considered all of the most important second-order nonlinearities in realistic asymmetric quantum wells and investigated the dependence of this nonlinear coefficient on the well geometries and compositions. The second-order susceptibility was investigated under the action of an electric field [42, 43]. The optimization of second-order susceptibility has been analyzed and it has been shown that the optimization can be achieved by the methods of band-gap engineering and optimizing the product of three dipole matrix elements [11, 13, 44, 45, 46, 47]. The second-order nonlinearities due to exciton and continuum states were also investigated [48].

Although high values of SHG associated with intersubband transitions are

obtained, there is a severe obstacle in getting high conversion efficiencies. This is the strong absorption of the pump (ω) and the doubled (2ω) signals [10, 11]. The saturation of the second-harmonic generation conversion efficiency was demonstrated by Boucaud *et al.* [49]. They obtained a conversion efficiency of 3.4×10^{-4} at the pump intensity of 16 MW/cm^2 . For larger values of the intensity the conversion efficiency started to decrease. Later, Chen *et al.* [50] obtained a conversion efficiency as large as 3×10^{-3} at the pump intensity of 2 MW/cm^2 . The works on SHG conversion efficiency have reached different conclusions due the mathematical complexity of the problem when the rotating wave approximation is used instead of the perturbative approach [11, 44, 51, 52, 53, 54]. Note that the perturbative approach is not applicable in case of strong pump intensities. DeTemple *et al.* [51] showed the full-resonance maximized SHG and they obtained large conversion efficiencies ($> 50\%$) on-resonance at high intensities attributed to the ac-Stark effect. But Boucaud and Julien [52] concluded that some detuning is needed to get high conversion efficiency (they obtained a conversion efficiency greater than 6% at the pump intensity of 10 MW/cm^2) contrary to the conclusion of DeTemple *et al.* [51]. Ikonić *et al.* [44] demonstrated a high conversion efficiency (20%) in a rectangular quantum well under dc-fields at double resonance. Rosencher [54] concluded that a large conversion efficiency 20% is possible at double resonance before the onset of saturation by solving the propagation equation numerically with perturbative coefficients. Almogly and Yariv [11, 55] showed that

an optimal conversion efficiency is available on double resonance at weak intensities while at higher intensities some detuning reduces the saturation. Vurgaftman *et al.* [56] found that a conversion efficiency of 2.6% at $I = 4.1 \text{ MW/cm}^2$ and 2.6% at $I = 15 \text{ MW/cm}^2$ using surface-incidence and waveguide-mode analysis SHG with detuned intersubband transitions in GaAs-AlGaAs quantum wells.

All the works cited above mainly focused on the quantum wells having intersubband transition energies around 100 meV and surface electron densities $< 10^{12} \text{ cm}^{-2}$. In such systems, the depolarization and exciton-like effects can be neglected because they bring relatively small corrections compared to the subband energy spacings. However, the exciton-like effect is important when the subband energy spacing is smaller than 100 meV at lower densities of electrons. Also, the depolarization effect should be included when the density of electrons is quite high. Bewley *et al.* [57] measured the nonresonant SHG in half semi-parabolic quantum wells having an intersubband transition energy in far-infrared region. They concluded that the electron-electron interaction should be fully included in calculations of SHG (a typical correction to the transition energy due to the depolarization and exciton-like effects is $\approx 10 \text{ meV}$ in such quantum wells). Heyman *et al.*[58] designed a double asymmetric quantum well approximated by the first two energy levels as the transition energy ($\approx 10 \text{ meV}$) from ground to the first excited state was much larger than those resulted from ground to the other excited states. They observed that the peak position occurred at an energy

a few meV larger than the bare intersubband energy and the spectrum was modified compared to the result obtained through one-electron approximation. They could explain these observations by including the depolarization effect into their calculations. Later, Załuźny [59] and Bondarenko and Załuźny [60] improved the SHG expression including both depolarization and exciton-like effects.

In this part of the work, we will calculate the second-order nonlinear optical properties of quantum wells described by the Pöschl-Teller confining potential. Since the potential itself has variable asymmetry parameters, we can work out the effects of the degree of the asymmetry on the second-order nonlinearities.

5.3 Second-Harmonic Generation in a Pöschl-Teller Quantum Well

As discussed previously, the asymmetry is the key point in the second-order nonlinearities. The Pöschl-Teller quantum well has an advantage of having a variable asymmetry whereas the other types of quantum wells have a definite shape of asymmetry determined by the growth conditions or a variable asymmetry but obtained through external-bias. Therefore, the Pöschl-Teller potential provides a possibility for determining the behavior of SHG in a quantum well with an adjustable asymmetry.

The expression for SHG for a two-level system is given by

$$\chi_{2\omega}^{(2)} = 2 \frac{\sigma_s |\mu_{10}|^2 (\mu_{11} - \mu_{00})}{E_{10}^2 - (\hbar\omega + i\hbar\Gamma_0)^2} \left[\frac{\hbar\omega + i\hbar\Gamma_0}{2\hbar\omega + i\hbar\Gamma_1} + \frac{E_{10}^2 + (2\hbar\omega + i\hbar\Gamma_0)(\hbar\omega + i\hbar\Gamma_0)}{E_{10}^2 - (2\hbar\omega + i\hbar\Gamma_0)^2} \right]. \quad (5.1)$$

assuming that the optical field is polarized in the growth direction of the quantum well, z , and only the ground state is occupied by the electrons, and the off-diagonal and diagonal elements of Γ_{nm} are equal to Γ_0 and Γ_1 , respectively. Here σ_s represents the electron concentration in the ground state. If the first three levels are used, we obtain the following expression

$$\zeta_{2\omega}^{(2)} = \frac{\sigma_s \mu_{10} \mu_{21} \mu_{02}}{[E_{10} - \hbar\omega + i\hbar\Gamma_0][E_{20} - 2\hbar\omega + i\hbar\Gamma_0]}. \quad (5.2)$$

This equation gives larger SHG peaks when the double resonance is met, that is when $E_{21} \approx E_{10} \approx \hbar\omega$ [13]. The ratio of the resonance values of both expressions yields

$$\left| \frac{\zeta_{2\omega,peak}^{(2)}}{\chi_{2\omega,peak}^{(2)}} \right| \approx \frac{1}{2} \left| \frac{\mu_{10} \mu_{21} \mu_{02}}{\mu_{10}^2 (\mu_{11} - \mu_{00})} \right| \frac{E_{10}}{\hbar\Gamma_0}. \quad (5.3)$$

Since E_{10} is much larger than $\hbar\Gamma_0$, $\zeta_{2\omega,peak}^{(2)} \gg \chi_{2\omega,peak}^{(2)}$, apart from the geometrical factor $|\mu_{10} \mu_{21} \mu_{02} / \mu_{10}^2 (\mu_{11} - \mu_{00})|$. But, in a quantum well described by the Pöschl-Teller potential equal spacing of energy levels is not possible (see Eq. (4.4)).

We display SHG spectrum of a quantum well described by the Pöschl-Teller potential as a function of the photon energy in Fig. (5.2) for $\kappa = 1.2, 1.9$ and 2.8 at $\eta = 2$, shown by dashed-, solid and dashed-dotted-lines, respectively. We take $\Gamma_1 = (1 \text{ ps})^{-1}$, $\Gamma_0 = (0.14 \text{ ps})^{-1}$ and $\sigma_s = 3 \times 10^{16} \text{ cm}^{-3}$. There is no applied electric field. Eq. (5.1) reveals two distinct peaks in the spectrum, occurring at $\hbar\omega \approx E_{10}/2$ and $\hbar\omega \approx E_{10}$, respectively. As κ increases the peaks decrease at first, become zero at $\kappa = 2.0$, for which the potential is symmetric, and increase

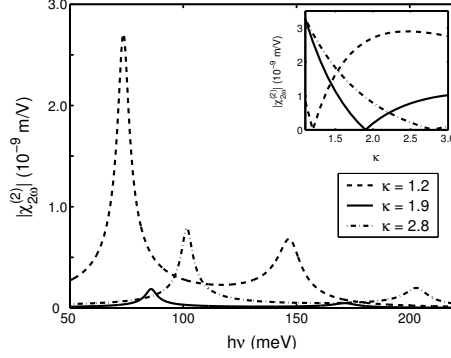


Figure 5.2: Second-harmonic generation as a function of the photon energy in a Pöschl-Teller quantum well. The solid, the dashed and the dotted-curves stand for $\kappa = 1.2$, $\kappa = 1.9$ and $\kappa = 3$, respectively. Inset displays the peak appearing at $\hbar\omega \approx E_{10}/2$ as a function of κ for $\eta = 1.2, 1.9$ and 2.8 , denoted by dashed-, solid and dashed-dotted-lines, respectively.

again. The maximum value of SHG attained is approximately 3 nm/V which is one order of magnitude larger than that in bulk GaAs. The peak positions are always blue-shifted in accordance with Eq (4.4).

The peak at $\hbar\omega \approx E_{10}$ is very weak compared with the other one. This can be checked easily using Eq. (5.1), such that

$$\chi_{2\omega}^{(2)}(\hbar\omega \approx E_{10}/2) \propto \frac{1}{-E_{10}/2 + i\hbar\Gamma_0}, \quad (5.4)$$

and

$$\chi_{2\omega}^{(2)}(\hbar\omega \approx E_{10}) \propto \frac{1}{E_{10} + i\hbar\Gamma_0}, \quad (5.5)$$

where we retained only the resonance terms in Eq. (5.1). The absolute value of the ratio of Eq. (5.4) to Eq. (5.5) gives us 2. This is quite a large value. Therefore,

we may safely ignore the peak appearing at $\hbar\omega \approx E_{10}$. The inset of Fig. (5.2) shows the peak at $\hbar\omega \approx E_{10}/2$ as function of κ for $\eta = 1.2, 1.9$ and 2.8 , denoted by dashed-, solid and dashed-dotted-lines, respectively. As expected, the peak is zero along the line $\kappa = \eta$ which makes the Pöschl-Teller potential symmetric. But as they become different, the peak value grows and it reaches its maximum value when one of the parameters is the greatest while the other one is the smallest. This can be explained by the maximization of the difference $|\mu_{11} - \mu_{00}|$ since the well becomes very wide while it remains asymmetric in that case. The maximum value of SHG attained by changing the parameters does not exceed the previous value, approximately 3 nm/V . The result is much smaller than those obtained in the experiments or in the earlier theoretical studies. This can be explained by the absence of the double resonance and the smallness of $|\mu_{11} - \mu_{00}|$ (it is between $0 - 10 \text{ \AA}$) compared to those obtained in other quantum wells. It is four times larger in a step quantum well than the one obtained here [61].

Eq. (5.1) is displayed as function of the photon energy in Fig. (5.3) for the electric fields of $F = 25, 50$ and 100 kV/cm , denoted by dashed-, solid and dashed-dotted-lines, respectively. We take $\kappa = \eta = 2$. Initially, SHG is zero due to the symmetry of the potential (not shown), but it increases quickly because of the gradual increase in $|\mu_{11} - \mu_{00}|$ when the field is turned on. We say that the enhancement of SHG, as large as three times, is possible with the DC electric field. That is quite similar to the result obtained in a square quantum well under

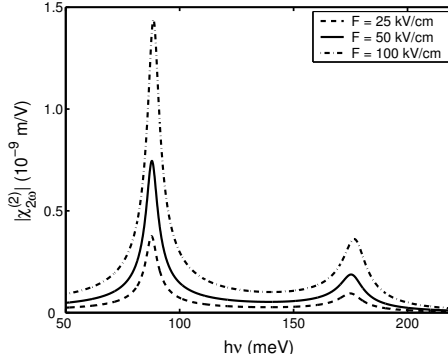


Figure 5.3: Second-harmonic generation as a function of the photon energy in a Pöschl-Teller quantum well under the electric field of $F = 25, 50$ and 100 kV/cm, denoted by dashed-, solid and dashed-dotted-lines, respectively. In the figure, $\kappa = \eta = 2$.

the electric field [42]. The peak position is blue-shifted with the increasing electric field.

In Fig. (5.4), we plot the peak occurring at $\hbar\omega \approx E_{10}/2$ in Eq. (5.1) as a function of the electric field, for the values of $\kappa = 2, 2.3, 2.6$ and 2.9 , denoted by solid, dashed-, dashed-dotted- and dotted-lines, respectively. In the figure, $\eta = 2$. Since the potential is symmetric when $\kappa = \eta$, the peak is zero at $\kappa = 2$ and $F = 0$ kV/cm but it starts to increase as F increases. However, for the values of $\kappa \neq 2$, the peak value becomes zero at specific electric field strengths, such as at $F \cong 35$ kV/cm for $\kappa = 2.3$. In other words, quenching of SHG is possible at fixed κ, η by applying the electric field. In a similar fashion, it is shown that the quenching of SHG with the applied electric field is possible in a compositional

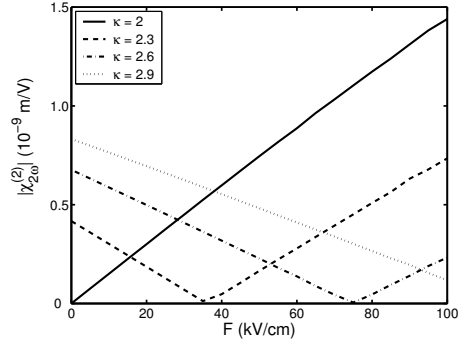


Figure 5.4: The peak, appearing at $\hbar\omega \approx E_{10}/2$ in the expression of SHG, as a function of the electric field for the values of $\kappa = 2, 2.3, 2.6$ and 2.9 , denoted by solid, dashed-, dashed-dotted- and dotted-lines, respectively. $\eta = 2$ in the figure.

asymmetric coupled quantum well by Huang *et al.* [62].

As a result, we may say that a large SHG peak is possible in a Pöschl-Teller quantum well when its parameters are kept as small as possible. A large enhancement in the peak value of SHG can be possible by the electric field provided that the parameters are kept smaller. Whereas the SHG obtained here is comparably larger than that in a bulk GaAs, it is much smaller than that obtained either experimentally or theoretically in the similar quantum wells. As discussed in the text, the main reasons are the absence of the double resonance and the smallness of the quantity, $|\mu_{11} - \mu_{00}|$. An interesting point is that the electric field can make SHG peak disappear. This dual behavior of the potential is due to its controllable asymmetry through its parameters.

5.4 Optical Rectification

The coefficient of the constant term (that is $\frac{1}{2}\chi^{(2)}E^2$ in Eq. (3.3)) which contributes zero frequency in the SHG expression is the optical rectification (OR) coefficient. It is the creation of a static electric field in the material due to the incident optical field. Optical rectification is observable only in noncentrosymmetric systems. The first observation of the optical rectification was done by Rosencher *et al.* [61] in a stepped GaAs/AlGaAs quantum well. They measured an optical rectification of 5.25×10^{-6} m/V which is three orders of magnitude higher than that of bulk GaAs at $10.6 \mu\text{m}$ resulted from the maximization of the product $|\mu_{10}|^2(\mu_{11} - \mu_{00})$ in the expression of optical rectification derived for a two-level system. Later, Rosencher *et al.* [63] observed a larger value of the OR coefficient, as large as 1.62×10^{-3} m/V at $8 - 12 \mu\text{m}$ range, observed in asymmetric GaAs/AlGaAs wells coupled by a weak intermediate potential barrier. The main reason was the long lifetime of the electrons in a metastable level slowly interacting with the ground state. Unterrainer *et al.* [64] measured an optical rectification coefficient of the order of 10^{-3} m/V at 11 meV, that is in far-infrared region, in doped asymmetric GaAs/AlGaAs quantum wells coupled by a thin potential barrier.

The optimization of the OR coefficient in asymmetric quantum wells by the methods of band-gap engineering and optimizing the product $|\mu_{10}|^2(\mu_{11} - \mu_{00})$

have attracted great interest [13, 65, 66, 67]. The possibility of the OR coefficient in a biased parabolic quantum well was also shown [68].

Derivation of the expression for OR coefficient in a two-level system is straightforward. It is achieved by setting $\omega_s = -\omega$ and $\omega_r = \omega$ in Eq (3.21). After some mathematical manipulations, it may be written as,

$$\chi_0^{(2)} = 4 \frac{\sigma_s |\mu_{10}|^2 (\mu_{11} - \mu_{00})}{\hbar^2} \frac{\omega_{10}^2 \left[1 + \frac{\Gamma_0}{\Gamma_1}\right] + (\omega^2 + \Gamma_0^2) \left[\frac{\Gamma_0}{\Gamma_1} - 1\right]}{[(\omega - \omega_{10})^2 + \Gamma_0^2][(\omega + \omega_{10})^2 + \Gamma_0^2]}. \quad (5.6)$$

In deriving the equation above, we assume that the optical field is polarized in the growth direction of the quantum well, z , and only the ground state is occupied by the electrons whose concentration is denoted by σ_s , and the off-diagonal and diagonal elements of Γ_{nm} are taken equal to Γ_0 and Γ_1 , respectively.

The maximum value of the OR coefficient is obtained at the resonance condition, $\hbar\omega \approx E_{10}$,

$$\chi_0^{(2)} = 2 \frac{\sigma_s |\mu_{10}|^2 (\mu_{11} - \mu_{00})}{\hbar^2} T_1 T_0 \quad (5.7)$$

assuming that $\Gamma_0, \Gamma_1 \ll \omega_{10}$. Hence the maximization of the OR coefficient will require a tradeoff between μ_{10} and $\mu_{11} - \mu_{00}$ and the enhancement of the lifetime of electrons, i.e. T_1 , in the excited state[13]. Because any increase in the asymmetry of the quantum well will increase the difference $\mu_{11} - \mu_{00}$ but decrease μ_{10} .

Eq. (5.6) is displayed as function of the photon energy in Fig. (5.5) for $\kappa = 1.2, 1.9$ and 2.8 at $\eta = 2$, shown by dashed-, solid and dashed-dotted-lines, respectively. Inset shows the peak value as a function of κ for several values of

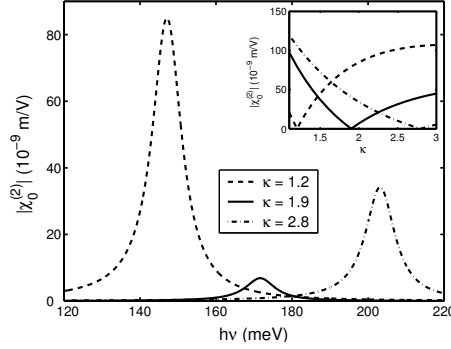


Figure 5.5: Optical rectification as a function of the photon energy in a Pöschl-Teller quantum well. The solid, the dashed and the dotted-curves stand for $\kappa = 1.2$, $\kappa = 1.9$ and $\kappa = 2.8$, respectively. Inset displays the peak as a function of κ for $\eta = 1.2, 1.9$ and 2.8 , denoted by dashed-, solid and dashed-dotted-lines, respectively.

η . As the potential becomes symmetric around $\kappa = \eta$, the peak value yields zero at $\kappa = \eta$. Generally speaking, the larger peaks are obtainable when one of the parameters is much smaller than the other one. By this, the maximum OR value is around 1.5×10^{-7} m/V, three orders of magnitude larger than that of bulk GaAs. Smallness of $\mu_{11} - \mu_{00}$ compared to that in a stepped well [61] is the main reason for the absence of the larger values of the OR coefficient here.

Eq. (5.6) is displayed as function of the photon energy in Fig. (5.6) for the electric fields of $F = 25, 50$ and 100 kV/cm, denoted by dashed-, solid and dashed-dotted-lines, respectively. We take $\kappa = 2$ and $\eta = 2.0$ in the figure. Since the potential becomes symmetric for $\kappa = \eta$, the OR coefficient is zero at zero bias. When the symmetry of the potential is broken down by the electric field, the

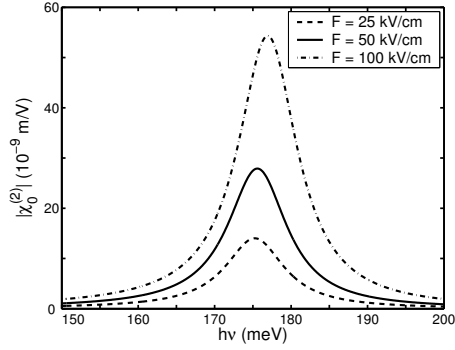


Figure 5.6: Optical rectification as a function of the photon energy in a Pöschl-Teller quantum well under the electric field of $F = 25, 50$ and 100 kV/cm, denoted by dashed-, solid and dashed-dotted-lines, respectively. In the figure, $\kappa = \eta = 2$.

OR coefficient gradually enhances. It is possible to enhance it as much as three times. A further increase in the peak value with the increasing electric field is possible by making one of the parameters as small as possible while keeping the other one as larger as possible. The peak position is slightly blue-shifted with the increasing electric field (see Fig. (4.3)).

We plot the peak as a function of electric field in Fig. (5.7) for the values of $\kappa = 2, 2.3, 2.6$ and 2.9 , denoted by solid, dashed-, dashed-dotted- and dotted-lines, respectively. In the figure, $\eta = 2$. The response of the peak to the changes in the electric field is very similar to that of SHG peak. An extinguishing OR coefficient is possible by varying the electric field provided that both κ and η are kept fixed. The strength of the electric field for this depends on the values of the parameters. We say that a larger electric field is required to make the

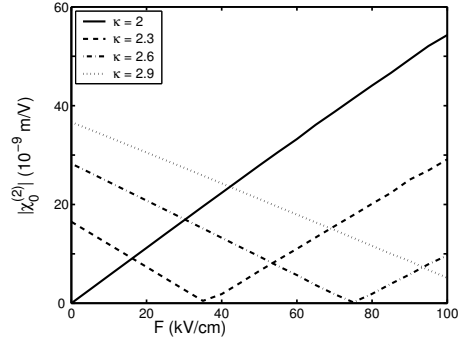


Figure 5.7: The peak in the expression of OR as a function of the electric field for the values of $\kappa = 2, 2.3, 2.6$ and 2.9 , denoted by solid, dashed-, dashed-dotted- and dotted-lines, respectively. $\eta = 2$ in the figure.

OR coefficient vanish as both parameters increase. This is physical because the electric field makes the well larger in contrast to what the increasing parameters do. The larger peak values are available at smaller κ .

In conclusion, a large OR peak is possible in a Pöschl-Teller quantum well when one of its parameters are kept as small as possible. A large enhancement in OR peak is possible when an electric field is applied. The effect of the field is more pronounced when one of the parameters is smaller than the other one. The electric field can make OR peak disappear. This interesting behavior of the potential is due to its controllable asymmetry through its parameters.

CHAPTER 6

THIRD-ORDER NONLINEARITIES

6.1 Introduction

In this chapter, we focus on the third-order nonlinear properties of a Pöschl-Teller quantum well, such as nonlinear intersubband absorption [29, 69], third-harmonic generation and intensity-dependent refractive index [70]. We aim to understand the changes in the third-order nonlinearities in a quantum well with an adjustable asymmetry, which is represented by the Pöschl-Teller quantum well. The nonlinear intersubband absorption is considered within the rotating wave approximation, in which the resultant absorption expression reduces to the one obtained when the density matrix equation is solved perturbatively. Third-harmonic generation and intensity-dependent refractive index are considered within the perturbational treatment of the density matrix equation given in Chapter III. The Coulomb and many-body effects are ignored in the calculations. We also include the DC electric field in our calculations. Numerical results are

presented for a wide range of the parameters of the potential.

6.2 Nonlinear Intersubband Absorption

Dingle *et al.* [1] in 1974 proved experimentally the existence of quantized states in a semiconductor quantum well. This was achieved by optical bandgap spectroscopy in a GaAs/AlGaAs structure. The possibility of infrared light detector based on intersubband transitions in quantum wells were shown by Esaki and Sakaki [3] and Smith *et al.* [4]. However, the first experimental report on the intersubband absorption in a GaAs/AlGaAs quantum well was presented by West and Eglash [2]. In their systems, the absorption peak occurred around $10\ \mu\text{m}$. This wavelength was in infrared region which is technologically important. The other observations of the experiment were the narrow bandwidth of the absorption and the large value of the dipole matrix element. That large dipole matrix element suggests a large value of third-order nonlinearities which depend on the fourth power of the dipole (see Eq. (3.22)). A great deal of effort, both theoretical and experimental, is devoted to intersubband transitions in quantum wells following the work of West and Eglash [2]. Most of them were motivated by the high technological potential of intersubband transitions for novel infrared detectors, emitters, and nonlinear optical elements (see Liu[5] for an excellent review of the device applications of intersubband transitions).

The first theoretical attempts on the investigation of the nonlinear absorption

associated with intersubband transitions in quantum wells were done by Yuen [71] and Ahn and Chuang [72]. Ahn and Chuang used the density matrix formalism including the intrasubband relaxation time. They assumed infinite quantum well having two energy levels. They obtained a decreasing absorption peak with the increasing intensity of the optical field.

Pöschl-Teller potential has adjustable parameters, providing a variable asymmetry. Therefore, it is fruitful to consider the nonlinear intersubband absorption spectrum, in which the asymmetry plays an important role.

6.3 Nonlinear Intersubband Absorption in a Pöschl-Teller Quantum Well

The absorption coefficient in terms of the susceptibility is

$$\alpha(\omega) = \frac{4\pi\omega}{c} \text{Im}[\chi(\omega)] \quad (6.1)$$

The linear and nonlinear absorption coefficients are defined as the contribution of $\chi^{(1)}(\omega)$ and $\chi^{(3)}(\omega)$ to Eq. (6.1), respectively. That can be obtained through Eq. (3.20) and Eq. (3.22). The result is

$$\alpha^{(1)}(\omega) = \frac{4\pi\omega}{n_r c} \frac{\sigma_s \mu_{10}^2 \hbar \Gamma_0}{(E_{10} - \hbar\omega)^2 + \hbar^2 \Gamma_0^2}, \quad (6.2)$$

$$\alpha^{(3)}(\omega) = -2\omega \left(\frac{4\pi}{n_r c} \right)^2 \frac{I \sigma_s \mu_{10}^4 \hbar \Gamma_0}{[(E_{10} - \hbar\omega)^2 + \hbar^2 \Gamma_0^2]^2}, \quad (6.3)$$

respectively. Here, I is the intensity of the incident field and $E_{10} = E_1 - E_0$.

We assume that only the ground state is populated which is given by σ_s and

that all elements of Γ_{nm} are equal to a single value Γ_0 . In deriving the equation above, we have deliberately ignored the term proportional to $|\mu_{11} - \mu_{00}|^2$ arising only in an asymmetric quantum well [73], since it is proportional to $(\hbar\Gamma_0)^2/E_{10}^2$ at resonance (for a typical quantum well $[\hbar\Gamma_0/E_{10}]^2 \ll 1$). We write the total absorption coefficient $\alpha(\omega, I)$ as

$$\alpha(\omega, I) = \alpha^{(1)}(\omega) + \alpha^{(3)}(\omega, I). \quad (6.4)$$

Eq. (6.4) is valid only in cases such that $I \ll I_s$ where I_s is the saturation intensity and is given by $I_s = c\epsilon^{1/2}\hbar^2\Gamma_1\Gamma_2/8\pi|\mu_{10}|^2$. Here Γ_1 and Γ_2 are the diagonal and off-diagonal elements of the Γ_{nm} , respectively. When I is comparable to or larger than I_s , within the rotating wave approximation (in the rotating wave approximation, only the terms close to resonance with the one of the optical frequencies in Eq. (3.9) are kept. For details, see Refs.[11, 23]), the result is [11, 74]

$$\alpha(\omega, I) = \frac{4\pi\hbar\omega\sigma_s\mu_{10}^2}{n_r c} \frac{\hbar\Gamma_2}{\left[(\hbar\omega - E_{10})^2 + \hbar^2\Gamma_2^2(1 + I/I_s)\right]}. \quad (6.5)$$

It is easy to show that Eq. (6.5) reduces to Eq. (6.4) when $\Gamma_1 = \Gamma_2 = \Gamma_0$ at $I \ll I_s$. But, equating diagonal and off-diagonal relaxation times to a single constant value is quite wrong since $\Gamma_2 \gg \Gamma_1$ for quantum wells having E_{10} much larger than LO phonon energy. Typical values are $\Gamma_1^{-1} = 1$ ps and $\Gamma_2^{-1} = 0.2$ ps [13]. When this is neglected, the saturation effect is substantially overestimated [11] (it gives saturation intensities considerably larger than those obtained in

experiments [11]: experimentally measured I_s are well below 1 MWcm^{-2} whereas one calculates $I_s > 1 \text{ MWcm}^{-2}$ using $T_1 = T_2 = 0.14 \text{ ps}$).

The peak value of Eq (6.5) occurring at $\hbar\omega = E_{10}$ reads

$$\alpha(I)_{peak} = \frac{\alpha(I=0)_{peak}}{1 + \frac{I}{I_s} \frac{|\mu_{10}|^2(\kappa, \eta)}{|\mu_{10}|^2(2, 2)}} \quad (6.6)$$

where $\alpha(I=0)_{peak}$ means Eq (6.5) is evaluated at $I=0$ and $\hbar\omega = E_{10}$. Note that I_s is a function of the $\mu_{10}(\kappa, \eta)$. In Eq (6.6), I_s is the saturation intensity evaluated at $\kappa = \eta = 2$.

In intersubband transitions most of the oscillator strength is in the $0 \rightarrow 1$ transition (it is nearly 0.96 for an infinite well potential). Then, the Thomas-Reich-Kuhn sum rule yields [13]

$$\frac{2m^*}{\hbar^2} E_{10} |z_{10}|^2 \cong 1. \quad (6.7)$$

That is, the enhancement of the linear absorption originates from the contribution of the optical transitions between the conduction band and the other bands of the quantum well [13]. Therefore, $\alpha(I=0)_{peak}$ which is proportional to $E_{10}|z_{10}|^2$ apart from some constants can not be enhanced over the variations in κ and η . However, the variations in Eq (6.6) with κ and η can be investigated as a function of the intensity within its limits, $[0, \alpha(I=0)_{peak}]$.

Fig. (6.1) shows the ratio $\alpha(I=I_s)_{peak}/\alpha(I=0)_{peak}$ as function of κ for $\eta = 1.2, 2$ and 2.8 . In the same figure, the ratio under an electric field of 100 kV/cm is also displayed with the same lines but marked with triangles. The ratio increases

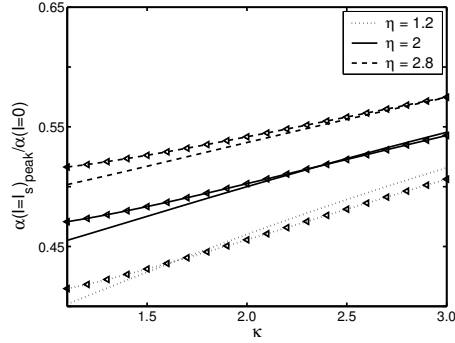


Figure 6.1: $\alpha(I = I_s)_{peak}/\alpha(I = 0)_{peak}$ as a function of κ . The dotted-, solid and dashed-lines stand for $\eta = 1.2$, $\eta = 2$ and $\eta = 2.8$, respectively while the same lines marked with triangles represent the case in which $F = 100$ kV/cm.

as κ and η increase. Since μ_{10} is linearly proportional to the well width, it decreases with the increasing κ and η which makes the well narrower. Therefore, $\alpha(I)_{peak}/\alpha(I = 0)_{peak}$ increases (see Eq. (6.6)).

There is no need to plot the transition energy since it can be stated in a simple analytical form. Using Eq. (4.4), it is easy to obtain

$$E_{10} = 2\hbar^2\beta^2(\kappa + \eta + 1). \quad (6.8)$$

Obviously, the equation above states the linear dependence of the transition energy on the potential parameters.

Since the saturation intensity is proportional to $|\mu_{10}|^{-2}$, any increase in the parameters, leading to decrease in the $|\mu_{10}|^2$, enhances the saturation intensity. Therefore, the intersubband absorption in a Pöschl-Teller quantum well saturates

earlier at smaller values of its parameters, κ and η .

6.4 Quantum-Confined Stark Effect

In 1987, Harwitt and Harris [75] observed a blue-shift of the intersubband absorption corresponding to the quantum-confined Stark effect in a GaAs/AlGaAs quantum well in an electric field of 36 kVcm^{-1} . The intersubband absorption was decreased and its linewidth was increased by the application of the electric field. Actually, this blue-shift was guessed theoretically by Bastard *et al.* [76] using the second-order perturbation theory in 1983. They concluded that the energy level of the first excited state remained almost unperturbed while that of the ground state was shifted down by an amount $\Delta E_0 = -0.0022(m^*q^2F^2L^4/\hbar^2)$. The behavior of the energy levels under an electric field but not in perturbative regime was investigated variationally [30, 76] and by the usual numerical methods [77, 78].

We have investigated the effect of the electric field on the intersubband absorption in a Pöschl-Teller quantum well variationally. The details of the calculation are given in Chapter 4. Here, we only display the results on the absorption lineshape and its peak value.

Table 4.1 shows the resonance energy ($\hbar\omega \approx E_{10}$ in parenthesis) for several values of κ and electric field, F . With the application of the electric field there occurs a shift in E_{10} but the sign of this shift depends strongly on the relative

values of the parameters with respect to each other. Generally speaking, we see that when $\eta < \kappa$ there is a blue-shift while in the opposite case there is a red-shift as shown in the table.

We plot the ratio $\alpha(I = I_s)_{peak}/\alpha(I = 0)_{peak}$ in Fig. (6.1) as a function of κ for several η (lines marked with triangles) at $F = 100$ kV/cm. It is obvious that the ratio increases fast for small values of the parameters and it approaches to a constant value for the large values of the parameters. The application of the electric field does not result in considerable changes. In general, it decreases the ratio when $\eta > \kappa$ and increases it when $\eta < \kappa$.

6.5 Third-Harmonic Generation

Third-order susceptibility, $\chi_{(\omega_q+\omega_s+\omega_r,\omega_q,\omega_s,\omega_r)}^{(3)}$, has attracted a growing interest in recent years. Walrod *et al.* [79] measured a resonantly enhanced third order susceptibility of $\chi_{(\omega,\omega,-\omega,\omega)}^{(3)} = 5.6 \times 10^{-13} \text{ m}^2/\text{V}^2$ in GaAs/AlGaAs superlattices at around $\lambda = 11 \mu\text{m}$ using nearly-degenerate four-wave mixing. Sirtori *et al.* [80] measured a triply resonant third-harmonic generation in coupled AlInAs/GaInAs quantum wells as high as $|\chi_{(3\omega,\omega,\omega,\omega)}^{(3)}| = 1.0 \times 10^{-14} \text{ m}^2/\text{V}^2$ at around $\lambda = 11 \mu\text{m}$. This value was enhanced to $|\chi_{(3\omega,\omega,\omega,\omega)}^{(3)}| = 4.0 \times 10^{-14} \text{ m}^2/\text{V}^2$ at low temperatures (30 K) by Capasso *et al.* [45]. Heyman *et al.* [58] observed a third-harmonic

generation in far infra-red region. Lien *et al.* [81] calculated third-harmonic generation for a compositional asymmetric coupled quantum well including energy-band nonparabolicity. Third-harmonic generation was calculated also for finite parabolic quantum wells [82]. Załużny [83] investigated theoretically the influence of the depolarization effect on third-harmonic generation in quantum wells. Whereas many effects in third-harmonic generation have been investigated, effects of variable asymmetry on third-harmonic generation is not studied. Pöschl-Teller quantum well can be a good candidate for such an investigation. This is what we do in this part of the work.

When Eq. (3.22) is expanded for a four-level system and only the resonance terms are kept, one obtains the following expression

$$\chi_{3\omega}^{(3)} = \frac{q^4 \sigma_S z_{10} z_{21} z_{32} z_{03}}{(E_{10} - \hbar\omega - i\hbar\Gamma_0)(E_{20} - 2\hbar\omega - i\hbar\Gamma_0)(E_{30} - 3\hbar\omega - i\hbar\Gamma_0)}, \quad (6.9)$$

assuming that all input frequencies are equal to a single value, i.e. $\omega_q = \omega_s = \omega_r = \omega$. This is the expression for third-harmonic generation (THG). In deriving the equation above, it is assumed that only the ground state is populated (denoted by σ_s), and all elements of Γ_{nm} are considered to be equal to a single value Γ_0 . THG expression has its maximum value when the triple resonance condition is met, that is in the case of equal energy spacings.

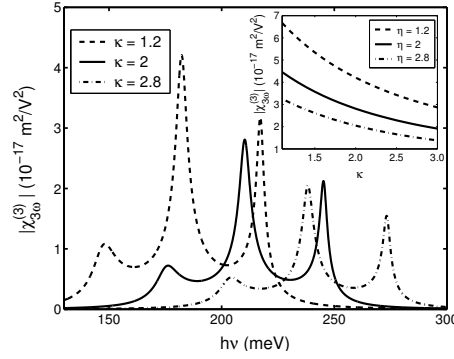


Figure 6.2: Third-harmonic generation as a function of the photon energy in a Pöschl-Teller quantum well. The dashed-, solid and dashed-dotted curves stand for $\kappa = 1.2$, $\kappa = 2$ and $\kappa = 2.8$, respectively. Inset displays the peak appearing at $\hbar\omega \approx E_{20}/2$ as a function of κ for $\eta = 1.2, 2$ and 2.8 , denoted by dashed-, solid and dashed-dotted-lines, respectively.

6.6 Third-Harmonic Generation in a Pöschl-Teller Quantum Well

We show the results for THG in a quantum well described by the Pöschl-Teller potential, including the electric field effects.

Eq. (6.9) is displayed as a function of the photon energy for several values of κ in Fig. (6.2). In the figure, $\eta = 2.0$. Since for such a potential the energy levels are not equally spaced, there appears three peaks, different in amplitude, instead of a huge single one. The maximum value attained is of the order of $10^{-17} \text{m}^2/\text{V}^2$, smaller than the other experimental [45, 79, 80] or theoretical findings [81, 82], although the dipole product $z_{10}z_{21}z_{32}z_{03}$ in Eq. (6.9) is comparable to the ones obtained in the other works [45, 80]. The reason is the absence of the triple

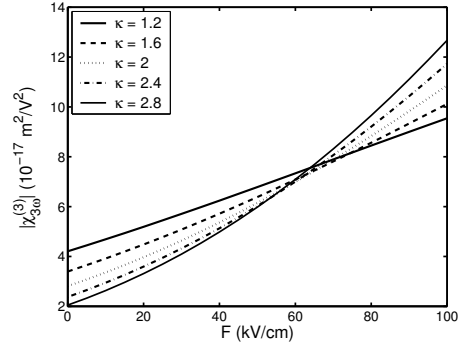


Figure 6.3: The peak, appearing at $\hbar\omega \approx E_{20}/2$ in the expression of THG, as a function of the electric field for the values of $\kappa = 1.2, 1.6, 2, 2.4$ and 2.8 . $\eta = 2$ in the figure.

resonance in Eq. (6.9). The peak positions are blue-shifted with increasing κ in accordance with Eq. (4.3). The inset shows the peak occurring at $E_{20}/2$ as a function of κ for the various values of η . As it is clearly, the maximum THG value, available at $E_{20}/2$, is enhanced as both of the parameters are kept smaller.

The peak at $E_{20}/2$ is shown as a function electric field at $\eta = 2$ for several values of κ in Fig. (6.3). Generally, the peak value increases as the electric field increases. However, it decreases with the increasing κ up to $F \approx 65$ kV/cm at fixed F . Beyond this value of the field, the situation is reversed: the smaller the κ the larger the peak at fixed F . This may be due to the complicated competition between the electric field and the parameters, κ and η in determining degree of the asymmetry of the potential. The Pöschl-Teller quantum well gives rather small values for THG. The main reason is the nonexistence of the triple resonance

in the energy levels. As κ and η decrease THG enhances. The electric field makes THG increase for all values of the asymmetry parameters.

6.7 Intensity-Dependent Refractive Index

The intensity of the optical field incident on an optical material changes the refractive index of the corresponding material. The intensity-dependent change in the refractive index in turn affects the propagation of the optical beam in the material, leading to the novel nonlinear optical effects. Among them, we can mention 'self-focusing of light', 'optical phase conjugation', 'optical bistability and optical switching' and 'two-beam coupling', details of which can be found in advanced nonlinear optics textbooks [23, 25].

The refractive index of quantum wells have been studied extensively [56, 84, 85, 86, 87, 88, 89, 90, 92, 91, 93, 94]. In the works cited above, changes in the refractive index associated with the interband and intersubband transitions in various quantum wells, such as parabolic and semiparabolic [86, 92, 93, 94], square [85, 88, 89], asymmetric single [87] and double quantum wells [56], have been investigated. Recently, intensity-dependent refractive index change has been measured for bulk GaAs [90, 95, 96, 97] and GaAs/AlGaAs quantum wells [91]. Whereas, the works cited above considered the effect of the asymmetry on the change in the refractive index, they confined their studies to the fixed kind of

asymmetry obtained through either band-gap engineering or external fields. However, a potential having adjustable asymmetry was not used. The Pöschl-Teller potential is suitable to investigate the influence of the asymmetry.

The expression for the frequency-dependent refractive index of a dilute system is approximated as

$$n_r(\omega) = n_r \sqrt{1 + 4\pi \frac{\text{Re}[\chi(\omega)]}{n_r^2}} \cong n_r \left(1 + 2\pi \frac{\text{Re}[\chi]}{n_r^2}\right), \quad (6.10)$$

where n_r is the bulk refractive index. Therefore, the change in the refractive index is

$$\Delta n_r(\omega) = 2\pi \frac{\text{Re}[\chi(\omega)]}{n_r}. \quad (6.11)$$

Using the rotating wave approximation, $\chi(\omega)$ for a two-level system is given by [11, 23]

$$\chi(\omega) = \frac{4\pi\sigma_s\mu_{10}^2T_2}{\hbar} \frac{(\omega - \omega_{10})T_2 + i}{1 + (\omega - \omega_{10})^2T_2^2 + 4\Omega^2T_1T_2}, \quad (6.12)$$

where $T_{1(2)} = T_{11(22)}$ is the life-(dephasing) time, $\Omega = |\mu_{10}||E|/\hbar$ is the Rabi frequency. One can obtain the full expression for the intensity-dependent change in the refractive index by inserting Eq. (6.12) into Eq. (6.11).

At low intensities of the optical field, the expression given by Eq. (6.12) can be approximated, leading to the description of the change in the refractive index by $\chi^{(1)}(\omega)$ and $\chi^{(3)}(\omega)$, expressions of which are given by Eq. (3.20) and Eq. (3.22), respectively. In this case, the intensity-dependent change is described by $\text{Re}[\chi^{(3)}(\omega)]$. $\chi^{(3)}(\omega)$ can be achieved by the permutations of the frequency

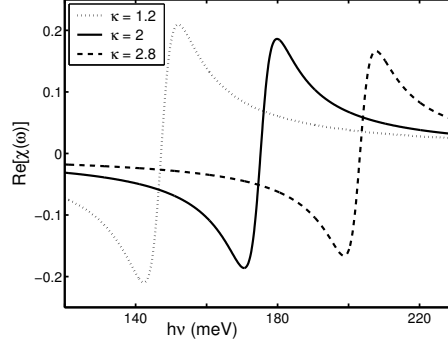


Figure 6.4: $\text{Re}[\chi(\omega)]$ as a function of the photon energy. The dotted-, solid and dashed-curves stand for $\kappa = 1.2$, $\kappa = 2$ and $\kappa = 2.8$, respectively.

set $(\omega, \omega, -\omega)$ in Eq. (3.22). The $\chi^{(3)}(\omega; -\omega, \omega, \omega)$ is dominant when the condition for two-photon resonance is met [88] while terms $\chi^{(3)}(\omega; \omega, -\omega, \omega)$ and $\chi^{(3)}(\omega; \omega, \omega, -\omega)$ are dominant at one-photon resonance. Then the result is

$$\chi^{(3)}(\omega) = \frac{2\pi I \sigma_s |\mu_{10}|^4}{n_r c (E_{10} - \hbar\omega - i\hbar\Gamma_0)} \times \left(\frac{4}{(E_{10} - \hbar\omega)^2 + (\hbar\Gamma_0)^2} - \frac{|\mu_{11} - \mu_{00}|^2}{|\mu_{10}|^2} \frac{1}{(E_{10} - \hbar\omega - i\hbar\Gamma_0)(E_{10} - i\hbar\Gamma_0)} \right), \quad (6.13)$$

for a two level system when only the resonant terms are kept and all the elements of Γ_{nm} are assumed to be equal to a single constant value Γ_0 . In the equation above, $I = n_r c |E|^2 / 2\pi$ is the intensity of the optical field.

We have plotted $\text{Re}[\chi(\omega)]$ as a function photon energy for a quantum well described by the Pöschl-Teller potential in Fig.(6.4) at $I = I_s$ (I_s is the saturation intensity and given by $I_s = c\epsilon_r^{1/2}\Gamma_1\Gamma_2/8\pi\mu_{10}^2$ where $\Gamma_{1(2)} = \hbar/T_{1(2)}$ is the diagonal

(off-diagonal) elements of Γ_{nm}). While η is fixed at 2.0, the parameter κ is taken to be 1.2, 2.0 and 2.8, denoted by dotted-, solid and dashed-lines in the figure, respectively. The amount of the change in the refractive index depends on the values of κ and η : a large change in the refractive index is possible at smaller values of the asymmetry parameters. The peaks of $\text{Re}[\chi(\omega)]$ occur at

$$\hbar\omega = \hbar\omega_{10} \pm \Gamma_2 \sqrt{I/I_s + 1}, \quad (6.14)$$

and they are

$$\text{Re}[\chi(\omega)]_{peak} = \pm \frac{1}{2} \frac{4\pi\sigma_s \mu_{10}^2}{\Gamma_2 \sqrt{I/I_s + 1}}. \quad (6.15)$$

The peak value is thus controlled by the dipole matrix element, μ_{10} . Since the larger values of the parameters yield a larger quantum well, which in turn enhances μ_{10} , we obtain larger changes in the refractive index. The results shown here are in accord with those obtained in the other works [56, 84, 85, 86, 87, 88, 89, 90, 92, 91, 93, 94].

The peak value of $\text{Re}[\chi(\omega)]$ is displayed as a function of κ for the several values of η in Fig.(6.5). In general, as the parameters decrease the change in the refractive index decreases. A simple explanation is the decrease in the μ_{10} value as the quantum well becomes narrower with the increasing κ and η . We may say that a possibly large change will occur when the potential parameters are as small as possible.

In conclusion, intensity-dependent refractive index is a strong function of the

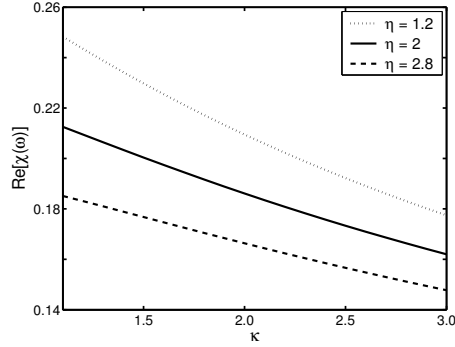


Figure 6.5: The peak value of $\text{Re}[\chi(\omega)]$ as a function κ . The dotted-, solid and dashed-curves stand for $\eta = 1.2$, $\eta = 2$ and $\eta = 2.8$, respectively.

shape of the potential. This is mainly due to the evolution of the dipole matrix element, μ_{10} , with the changes in the parameters. A large change in the refractive index is possible at smaller values of κ, η for which the Pöschl-Teller potential becomes wider. Since the wider quantum wells yield larger dipole matrix elements in magnitude (for an infinite quantum well $|\mu_{10}|^2 \propto L^2$), we obtain larger changes in the refractive index. The electric field does not affect the refractive index considerably unless κ and η are small enough.

CHAPTER 7

NONLINEAR INTERSUBBAND ABSORPTION OF δ -DOPED QUANTUM WELLS

7.1 Introduction

Now that we have studied a model potential profile in detail, we can go into a detailed study of a more realistic problem. For this, we have chosen a Si- δ -doped GaAs quantum well. Recent advances in epitaxial growth techniques, such as molecular beam epitaxy (MBE) make it possible to fabricate high quality Si δ -doped layers in GaAs quantum well (QW). The electrons supplied by Si atoms which are located in several atomic layers form a two-dimensional electron gas at high donor concentrations. Such QW structures have potential for device applications such as high-power FETs, and infrared devices, e.g. infrared detectors, modulators, and frequency converters, based on the intersubband transition of electrons.

In this part of the work, we investigate the nonlinear absorption spectra of a Si

δ -doped GaAs QW bounded by infinite barriers in the presence of the electric field [114]. We calculate the wave functions and energy levels of such Si δ -doped GaAs QW bounded by infinite barriers under an applied electric field by solving the Schrödinger and Poisson equations self-consistently. We calculate the nonlinear absorption line shape for various electric field strengths including the depolarization shift by the method introduced by Załużny [14]. We investigate how the nonlinear absorption spectrum depends upon the well width, sheet thickness and the electric field. We find strongly asymmetric absorption line shapes and redshifted peak positions when there is no electric field. But when the electric field is turned on, this asymmetry and redshift are decreased especially at relatively high field values, larger well widths, and thinner sheets.

7.2 Electronic Structure of δ -Doped Quantum Wells

7.2.1 Theoretical Description

Let N^{2D} and $a^* = \epsilon_r \hbar^2 / m^* e^2$ be the surface density of the donor atoms and the effective Bohr radius, respectively. When the heavy doping condition $N^{2D} a^* > 1$ is met in the plane of the layer, then all the donors are ionized completely. The total 2D-electron concentration will be equal to N^{2D} in this case. Together with the electrons, the donor atoms create a nonuniform electrostatic potential $\phi(z)$. Now the electrons are confined not by $V_B(z)$, the barrier potential, but also by the electrostatic potential energy, $-e\phi(z)$ in the growth direction, z . The resultant

confining potential has discrete energy levels, E_i . The whole energy spectrum of the quantum well is described by

$$E = E_i + \frac{\hbar^2 \mathbf{k}_\perp^2}{2m^*}, \quad (7.1)$$

where $\hbar \mathbf{k}_\perp$ is the in-plane momentum of the electron.

To understand the optical properties of the system, its main parameters should be calculated. This includes the confining potential, $V_B(z) - e\phi(z)$, the number of energy levels and their respective energies, E_i , and the corresponding wave functions $\psi(z)$ etc.

Described in the Hartree approximation, the electrostatic potential energy, $-e\phi(z) = V_H(z)$, created by the electrons and donors, satisfies the Poisson's equation

$$\frac{d^2 V_H(z)}{dz^2} = \frac{4\pi e^2}{\epsilon_r} (N_D^{3D}(z) - n(z)), \quad (7.2)$$

where ϵ_r is the local dielectric constant, $N_D^{3D}(z)$ and $n(z)$ are the three-dimensional donor and electron densities, respectively. $n(z)$ is given by

$$n(z) = \sum_i n_i |\psi_i(z)|^2, \quad (7.3)$$

where n_i represents the areal electron concentration in the i th subband and it is determined through

$$n_i = \frac{m^* kT}{\pi \hbar^2} \ln \left[1 + \exp \left(\frac{E_F - E_i}{kT} \right) \right] \quad (7.4)$$

in which the effective mass is taken as constant. The Fermi energy, E_F , is obtained as the solution of

$$N_D^{2D} = \sum_i n_i. \quad (7.5)$$

Coupled with Eq. (7.2), the Schrödinger equation,

$$\left[-\frac{\hbar^2}{2m^*} \frac{d^2}{dz^2} + V_b(z) + V_H(z) \right] \psi_n(z) = E_n \psi_n(z), \quad (7.6)$$

will provide us with the correct wave functions and the corresponding energy levels provided that both equations are solved self-consistently. However, there is no analytic solution to these coupled differential equations. In the following sections, therefore, we will adopt a numerical method to find out the wave functions and the energy levels.

7.2.2 Numerical Procedure

It is easier to handle numerically the equations when the dimensionless variables are introduced. We transform the well length, L , doping layer thickness, d , where we assume that $N_D^{3D} = N_D^{2D}/d$, and the position, z , with their reduced counterparts l , Δ , and x by using a^* [110]. The reduced energies ϵ , and the potentials v are introduced by rescaling E , and V with Ry^* (where $Ry^* = e^2/2\epsilon_r a^*$ is the effective Rydberg). The reduced electric fields f , charge densities, ν , and temperatures, τ are also introduced using the corresponding scaled values $F_0 \equiv Ry^*/ea^* \approx 5.91 \text{ kVcm}^{-1}$, $n_0 \equiv a^{*-3} \approx 10^{18} \text{ cm}^{-3}$, and $T_0 \equiv Ry^*/k \approx 67.7 \text{ K}$.

In view of this rescaling procedure, Eq. (7.2) becomes

$$\frac{d^2 v_H}{dx^2} = 8\pi \left[\nu^{3D}(x) - \nu(x) \right], \quad (7.7)$$

where $\nu^{3D}(x) = a^{*2} N^{2D} / \Delta$ for $|x| < \Delta/2$ and 0 otherwise. Eq. (7.3) reads

$$\nu(x) = \sum_i \nu_i |\xi_i(x)|^2. \quad (7.8)$$

in which ξ_i represents i th corresponding dimensionless wave function. Eq. (7.4)

reduces to

$$\nu_i = \frac{\tau}{2\pi} \ln \left[1 + \exp \left(\frac{\epsilon_F - \epsilon_i}{\tau} \right) \right]. \quad (7.9)$$

Finally the dimensionless Schrödinger equation is

$$\left[-\frac{d^2}{dx^2} + v_b(x) + v_H(x) + fx \right] \xi_i(x) = \epsilon_i \xi_i(x). \quad (7.10)$$

with the boundary conditions of $\xi_i(\pm l/2) = 0$.

We solve these dimensionless equations by the finite difference method. In brief, the dimensionless variable l is discretized with $N + 1$ mesh points and Eq. (7.7) and Eq. (7.10) are converted into a set of finite difference equations:

$$\frac{1}{h^2} [v_H(x_{i+1}) - 2v_H(x_i) + v_H(x_{i-1}))] = 8\pi [\nu_D^{3D}(x_i) - \nu(x_i)], \quad (7.11)$$

$$-\frac{1}{h^2} [\chi_j(x_{i+1}) - 2\chi_j(x_i) + \chi_j(x_{i-1}))] + v(x_i)\chi_j(x_i) = \epsilon_j \chi_j(x_i), \quad (7.12)$$

where $x_i = ih - l/2$ and $h = l/(N + 1)$ for $i = 0, 1, \dots, N + 1$, respectively.

The corresponding boundary conditions become $v_H(x_0) = v_H(x_{N+1}) = 0$ and $\chi_j(x_0) = \chi_j(x_{N+1}) = 0$, respectively[110].

The next section presents the results of the numerical method described above.

7.2.3 Results and Discussion

The electronic properties of a Si δ -doped GaAs QW bounded by infinite barriers have been investigated theoretically by many authors [22, 106, 107, 108, 109, 110, 111, 112]. Also there are many experiments considering the electronic band structure such as infrared absorption [98], Raman [99, 100, 101], and magnetotransport measurements [102, 103, 104, 105] in Si δ -doped GaAs QW (see Shik and Mezrin[19] and Harris [20] for an excellent review of the subject). Therefore, we show the numerical results restricted to some specific values of the parameters.

In this part of the work, the numerical parameters are taken as $m^* = 0.067m_0$, $\epsilon_r = 12.7$, $N_D^{2D} = 5 \times 10^{12} \text{ cm}^{-2}$, $d = 20 \text{ \AA}$, $L = 500 \text{ \AA}$. The temperature is kept constant at $T = 4.2 \text{ K}$. The electric field is restricted to change between $0 - 100 \text{ kVcm}^{-1}$. The higher electric fields may cause $\Gamma - X$ mixing[120] so it is safe to deal with lower values. We plot the confining potential with respect to the Fermi level in Fig. 7.1. In the absence of the applied electric field, it is in the form of characteristic V-shape potential. The calculated confining potential in the absence of the electric field approaches to zero at the limits of the well in accordance with [111] but not in line with [110]. In the same figure, we also show the confining potential in the presence of the electric fields of 50 kVcm^{-1} and 100 kVcm^{-1} . There is an obvious asymmetry introduced by the field. The field tends to lower the potential at the negative side of the z , thus we expect the distortion of the wave functions towards the negative side. This lowering of the

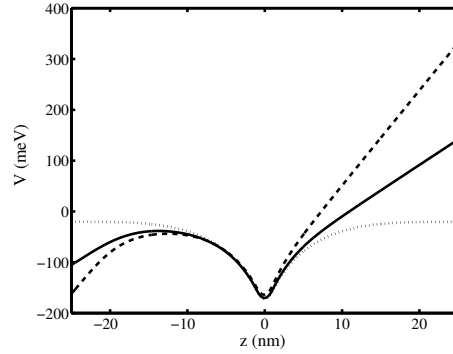


Figure 7.1: The confining potential from the self-consistent solution of the Schrödinger the Hartree equations with respect to the Fermi level for the applied electric fields of $F = 0 \text{ kVcm}^{-1}$ (dotted line), $F = 50 \text{ kVcm}^{-1}$ (solid line), and $F = 100 \text{ kVcm}^{-1}$ (dashed line).

confining potential is very much evident when the field strength is increased to 100 kVcm^{-1} as in Fig. 7.1. In fact there exists a secondary well at the negative side of z . However, there is no critical value of the electric field which cause a sudden decrease in the negative side of the confining potential, instead we see a monotonic lowering of the potential at the negative side of the well and a smooth formation of secondary triangular well as in [111].

The subband occupations are displayed as a function of applied electric field in Table 7.1. The ground state shows a weak electric field dependency while the other states, especially second and third excited states, are sensitive to the field. The interesting point is that the first excited state occupation first decreases and then increases with the field.

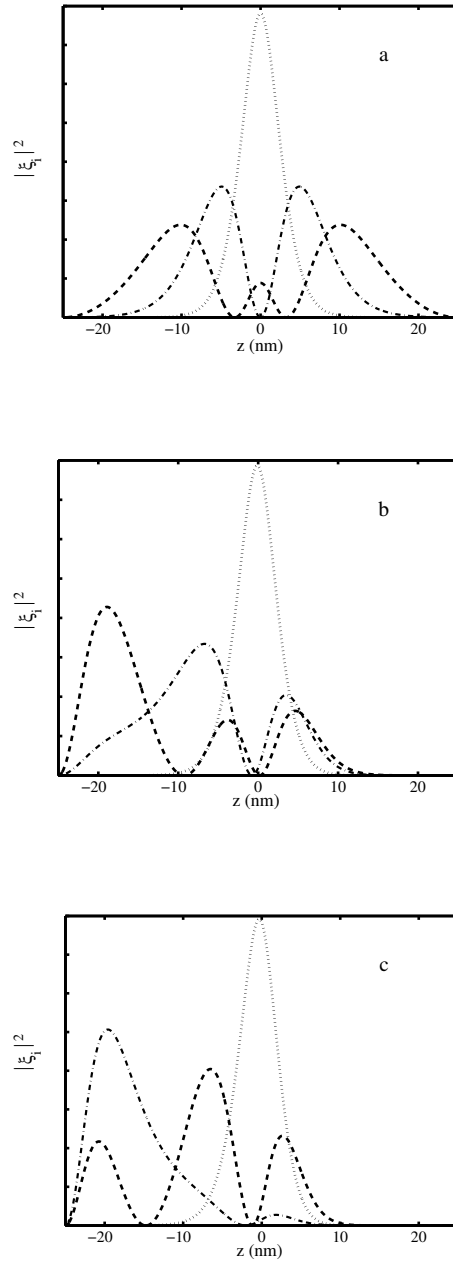


Figure 7.2: The squared wave functions of the ground (dotted-line), first excited (dashed-dotted), and the second excited (dashed line) subbands (a) in the absence of the electric field, (b) for the applied electric field of $F = 50 \text{ kVcm}^{-1}$, and (c) for the applied electric field of $F = 100 \text{ kVcm}^{-1}$.

Table 7.1: The calculated subband occupations in the unit of 10^{12} cm^{-2} for various electric fields.

$F \text{ (kVcm}^{-1}\text{)}$	n_1	n_2	n_3	n_4
0	3.064471	1.216462	0.578187	0.140869
50	2.996143	1.177147	0.765917	0.060800
100	2.796652	1.352324	0.851005	0.000000

We display the first three wave functions in Fig. 7.2(a)-(c) and their corresponding energy values from the Fermi level in Fig. 7.3. The zero-field wave functions are completely symmetric around $z = 0$ as expected. The ground state is localized in a narrower region than the excited states. When the electric field is turned on, the wave functions started to shift to the left side of the well as clearly seen in Fig. 7.2(b) and Fig. 7.2(c). This is obvious for the first and second excited states while ground state wave function is less distorted. At $F = 100 \text{ kVcm}^{-1}$, we see that the ground and first excited states are well separated. Fig. 7.3 shows that the corresponding energy levels except for the second excited subband energy are insensitive to the electric field especially up to $F = 50 \text{ kVcm}^{-1}$. The ground state and the first excited state energies move towards each other at higher electric fields. We did not observe any abrupt drop in energy levels at $F = 50 \text{ kVcm}^{-1}$ as pointed out in Ref.[110].

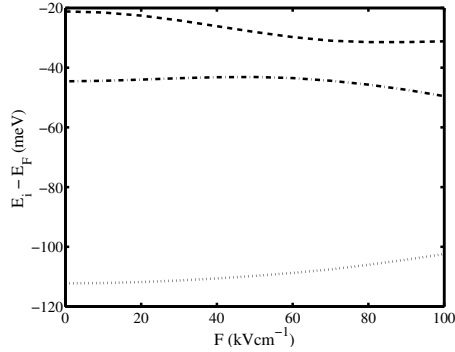


Figure 7.3: The energies of the ground (dotted line), the first excited (dashed-dotted line), and the second excited (dashed line) subbands with respect to the Fermi level as a function of the applied electric field.

7.3 Nonlinear Intersubband Absorption of δ -Doped Quantum Wells

There are a few theoretical works on the absorption properties of Si δ -doped GaAs QWs [108, 112, 113]. These concentrate on only the linear term in absorption coefficient and ignore the depolarization and exciton shifts except for Sasagawa *et al.* [113]. However, in such structures the depolarization and exciton shifts are not negligible [5] and the intersubband absorption process is modified by these effects [113]. The depolarization shift essentially comes from a (time-dependent) Hartree term related to the high-frequency field inducing the absorption. Each electron feels an effective field that is different from the external field by the mean Hartree field of the electrons polarized by the external field. Thus, the external field is screened by the quasi-two-dimensional electron

gas [5]. The exciton shift is due to the Coulomb interaction between the excited electron and the quasi-hole left behind in the ground state [5]. Zaluzny has calculated asymmetric and red-shifted nonlinear intersubband absorption line shape [14] for a rectangular GaAs QW when the depolarization effect is properly included. This is experimentally observed for modulation-doped rectangular GaAs QWs by Sherwin *et al.* [115] and Craig *et al.* [116].

The single particle description of the intersubband absorption,

$$\alpha(\omega, I) = \frac{4\pi\hbar\omega\sigma_s\mu_{10}^2}{n_r c} \frac{\hbar\Gamma_2}{[(\hbar\omega - E_{10})^2 + \hbar^2\Gamma_2^2(1 + I/I_s)]}. \quad (7.13)$$

is not adequate for the heavily-doped quantum wells [74]. A correct formulation must take into account the interaction between the electrons. In fact, the absorption process is affected by exciton and depolarization shifts in semiconductor heterostructures[5]. For example, the depolarization shift is found to enhance the transition energy by about 20% in a wide Si δ -doped QW [113]. Then the absorption maximum does not occur at the energy difference $E_{21} = E_2 - E_1$ but rather an energy given by[119]

$$\overline{E}_{21}^2 = E_{21}^2(1 + \alpha - \beta). \quad (7.14)$$

The quantities α and β (both > 0) are called depolarization and exciton shifts, respectively. Since both parameters are positive, the depolarization causes a

blue-shift while the exciton causes a redshift in the transition energy. The depolarization shift is calculated through

$$\alpha = \frac{8\pi e^2(n_1 - n_2)}{\epsilon_r E_{21}} \int_{-L/2}^{L/2} dz \left[\int_{-L/2}^z dz' \phi_2(z') \phi_1(z') \right]^2. \quad (7.15)$$

The exciton effect is given by

$$\beta = \frac{2(n_1 - n_2)}{E_{21}} \int_{-L/2}^{L/2} dz \phi_2^2(z) \phi_1^2(z) \frac{\partial V_{xc}(n(z))}{\partial n(z)}. \quad (7.16)$$

However, β is negligibly small in heavily-doped GaAs/AlGaAs systems[5]. Thus, we do not include it in the further calculations.

The effect of the depolarization shift on the linear absorption ($I = 0$) is just the replacement of the resonance energy E_{21} with \bar{E}_{21} [Eq. (7.14)], resulting in a blue-shift while keeping the lineshape unchanged. However, it is not such a straightforward task when $I \neq 0$. [14]. When the depolarization shift is properly included in the calculations, the absorption line becomes strongly asymmetric and the blue-shift in the transition energy provided by the depolarization shift is reduced [14]. This interesting phenomena has been experimentally observed for a 400 Å-wide GaAs QW modulation-doped by silicon layers of sheet density $1.3 \times 10^{12} \text{ cm}^{-2}$ which are placed 1250 Å from each side of the well by Sherwin *et al.* [115]. A possible reason is the significant population of the second subband through resonant excitation. Since when this occurs the absorption and the ability of the electrons to dynamically screen the exciting radiation is reduced. That results in a reduction in the depolarization shift and thus the peak position is

red-shifted towards to the bare peak position of the absorption line. As a result, the absorption line becomes asymmetric [115].

A brief mathematical description of the effects described above can be given as follows: The evolution of the density matrix $\rho(t)$ is given by

$$\frac{\partial \rho}{\partial t} = \frac{1}{i\hbar} [H_0 + H'(t), \rho] - R\rho, \quad (7.17)$$

where H_0 is the unperturbed Hamiltonian, and the $H'(t)$ is the effective perturbing Hamiltonian, and R is the relaxation operator. The relaxation operator is considered to have two distinct elements T_1 the intersubband relaxation time and T_2 the intrasubband relaxation time. Consider the the following form of the incident field

$$E(t) = \tilde{E}e^{-i\omega t} + \tilde{E}^*e^{i\omega t}. \quad (7.18)$$

Then the $H'(t)$ can be written as[14]

$$H'(t) = eE(t)z - \frac{4\pi e^2}{\epsilon_r} \int_{-\infty}^z dz' \int_{-\infty}^{z'} dz'' \Delta n(z'', t). \quad (7.19)$$

Here, the incident field $E(t)$ is considered to modify the density distribution of electrons and hence the Hartree potential. This is reflected by the change of the distribution, $\Delta n(z, t)$, in Eq. (7.19).

Within the rotating-wave approximation and restriction only to the steady-state responses, the nondiagonal matrix elements of $\rho(t)$ and $H'(t)$ are given by

$$H'_{ij}(t) = \tilde{H}'_{ij}(\omega)e^{-i\omega t} + \tilde{H}'_{ij}(-\omega)e^{i\omega t}, \quad (7.20)$$

$$\rho_{ij}(t) = \tilde{\rho}_{ij}(\omega)e^{-i\omega t} + \tilde{\rho}_{ij}(-\omega)e^{i\omega t}. \quad (7.21)$$

The absorption in a unit area is given by [14]

$$P(\omega, I) = \frac{1}{2}\text{Re}\tilde{\sigma}_{zz}(\omega, I)|\tilde{E}|^2, \quad (7.22)$$

where

$$\tilde{\sigma}_{zz}(\omega, I) = \frac{e^2(-i\omega)(n_1 - n_2)}{m^*} f_{21} \frac{W(\omega, I)H_{12}}{E_{21}^2 - (\hbar\omega)^2 - i2\hbar\omega\Gamma_2} \quad (7.23)$$

is the nonlinear conductivity and

$$W(\omega, I) = \left[1 + \frac{I}{I_0} \frac{|H_{12}|^2 2\Gamma_2^2 (E_{21}^2 + (\hbar\omega)^2)}{[E_{21}^2 - (\hbar\omega)^2]^2 + (2\hbar\omega\Gamma_2)^2} \right]^{-1}. \quad (7.24)$$

Here n_i is the corresponding subband occupation, f_{21} is the oscillator strength given by $2m_0(E_2 - E_1)/(|\langle\phi_2|z|\phi_1\rangle|^2\hbar^2)$, $H_{12} = \tilde{H}'_{12}(\omega)/\tilde{E}\mu_{12}$, $\Gamma_i = \hbar/T_i$, $I = c\epsilon_r^{1/2}|\tilde{E}|^2/2\pi$ is the intensity of the incident optical radiation, $I_0 = c\epsilon_r^{1/2}\Gamma_1\Gamma_2/8\pi e^2|\langle\phi_2|z|\phi_1\rangle|^2$ is the saturation intensity.

The H_{12} satisfies [14]

$$H_{12} \left[1 + \frac{\alpha E_{21}^2}{E_{21}^2 - (\hbar\omega)^2 - i2\hbar\omega\Gamma_2} W(\omega, I) \right] = 1. \quad (7.25)$$

For comparable intensities, Eq. (7.25) can be solved only numerically. But when $I \ll I_0$ one can obtain a simple analytical solution [14] to Eq. (7.25). In fact, when $\alpha = 0$ but I is still large, Eq. (7.23) together with Eq. (7.24) and Eq. (7.25) give Eq. (7.13).

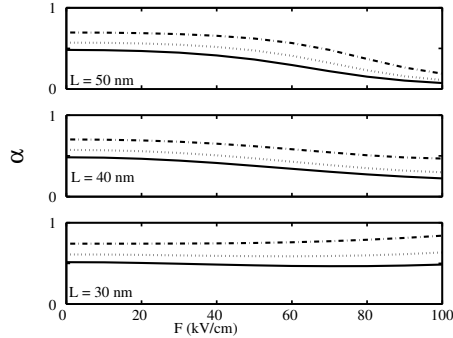


Figure 7.4: The depolarization shift α as a function of the electric field. The solid, dotted, and dashed-dotted lines stand for $\Delta z = 20 \text{ \AA}$, $\Delta z = 60 \text{ \AA}$, and $\Delta z = 100 \text{ \AA}$, respectively.

7.3.1 Results and Discussion

The numerical input parameters are taken as the same values with those in the previous section.

We first consider the importance of α for several values of the well width and sheet thicknesses under an electric field in Fig. 7.4. For a fixed L , it is clear that the sheet thicknesses has great influence on the depolarization shift for any value of the electric field: as the Δz increases α increases also. When L is changed there is no noticeable change in α at zero electric field. However, when the field is turned on, as L is decreased α increases significantly. This can be seen clearly for $L = 300 \text{ \AA}$. We have calculated also β , but we have found this shift to be very small. At most, it is less than 1% of α .

We show the transition energy \overline{E}_{21} together with E_{21} for several values of L

and Δz in Fig. 7.5. We observe that \overline{E}_{21} is always considerably greater than E_{21} for any value of L and Δz at relatively lower electric field strengths. At fixed well width, an increase in Δz results in a decrease in the transition energy since the potential barrier diminishes. This effect is clearly seen in the figure: larger Δz values yield smaller \overline{E}_{21} and E_{21} even though the depolarization shift is larger for the larger sheet thicknesses. If the well width is decreased the change in the transition energies at lower field values is not significant. But this is not the case for the higher field values: when $L = 300 \text{ \AA}$ both \overline{E}_{21} and E_{21} decreases more slowly than those for larger well widths with the electric field. Since the depolarization shift increases with the increasing electric field at $L = 300 \text{ \AA}$, the difference between \overline{E}_{21} and E_{21} is relatively high at $F = 100 \text{ kV/cm}$ compared to those at $L = 500 \text{ \AA}$.

We show the oscillator strength in the absence and the presence of the depolarization shift for various electric field values and sheet thicknesses in Fig. 7.6, Fig. 7.7, and Fig. 7.8 for the well widths of $L = 500 \text{ \AA}$, $L = 400 \text{ \AA}$, and $L = 300 \text{ \AA}$, respectively. The oscillator strength is a dimensionless quantity and it is important in all areas of optical spectroscopy since it facilitates the comparison of the transition strengths in different physical systems. The oscillator strength is enhanced with the inclusion of the depolarization shift. It improves further with the increase in the sheet thicknesses at constant well width. The effect of the decrease in the well width is to increase the oscillator strength. Especially at

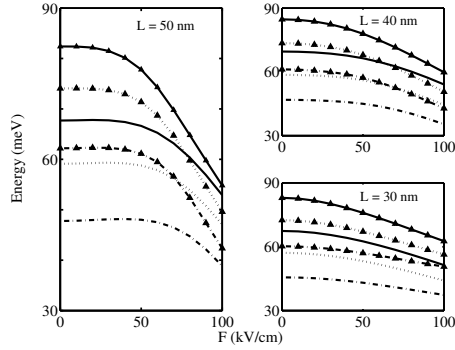


Figure 7.5: The intersubband transition energy with and without the depolarization shift as a function of the electric field. The solid, dotted, and dashed-dotted lines stand for $\Delta z = 20 \text{ \AA}$, $\Delta z = 60 \text{ \AA}$, and $\Delta z = 100 \text{ \AA}$, respectively. The lines marked with triangles represent the case in which the depolarization shift is included.

higher field values and sheet thicknesses this change is considerable.

The most important contribution to the oscillator strength comes from a region $\sim 200 \text{ \AA}$ around the doped layer where the wave function is most pronounced. This is quite insensitive to the electric field values $\leq 50 \text{ kV/cm}$. However, contribution of this region decreases significantly for the electric field values $\geq 50 \text{ kV/cm}$. Variations in L and Δz do not alter the above conclusion considerably.

The $\text{Re}\tilde{\sigma}_{zz}/\sigma_0$ is plotted as a function of photon energy at $I = I_0$ and $\Gamma_2 = 0.075E_{21}$ in Fig. 7.9, Fig. 7.10 and Fig. 7.11 for the well widths of $L = 500 \text{ \AA}$, $L = 400 \text{ \AA}$ and $L = 300 \text{ \AA}$, respectively. Here σ_0 stands for $(n_1 - n_2)e^2 f_{21}/2m^* \hbar \Gamma_2$ in which the numerical values belong to the zero-field case. In each figure, the Δz

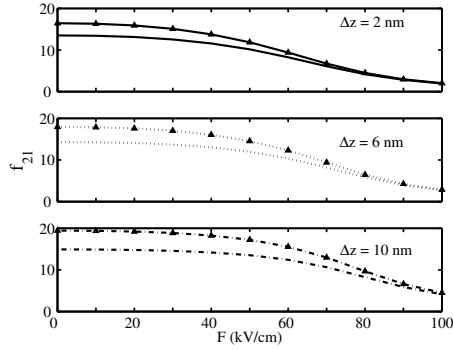


Figure 7.6: The oscillator strength with and without the depolarization shift as a function of the electric field for the well width of $L = 500 \text{ \AA}$. The lines marked with triangles represent the case in which the depolarization shift is included.

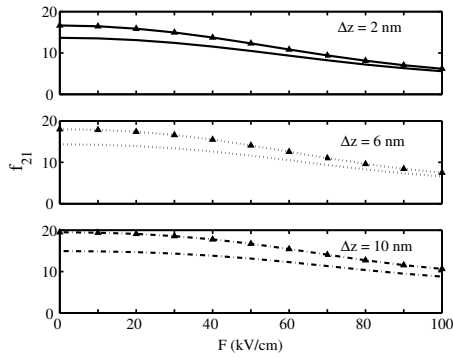


Figure 7.7: The oscillator strength with and without the depolarization shift as a function of the electric field for the well width of $L = 400 \text{ \AA}$. The lines marked with triangles represent the case in which the depolarization shift is included.

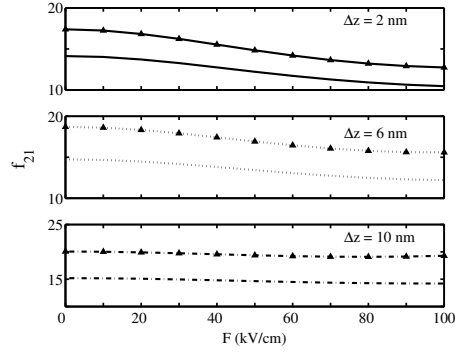


Figure 7.8: The oscillator strength with and without the depolarization shift as a function of the electric field for the well width of $L = 300 \text{ \AA}$. The lines marked with triangles represent the case in which the depolarization shift is included.

values are 20, 60 and 100 \AA while the F values are 0, 50 and 100 kVcm^{-1} , which are denoted by dashed-, dotted- and dashed-dotted lines respectively. The Fig. 7.9 reveals that the absorption line shape becomes strongly asymmetric and its peak value is reduced when a nonzero intensity (I_0) is applied. The peak position is red-shifted (i.e. it approaches to E_{21}) with respect to that of the absorption line shape at $I = 0$. A simple explanation is that the increase of the electron population in the first excited state which diminishes the ability of the electrons to dynamically screen the excitation radiation, leading to poor depolarization shifts. When the electric field is applied to the quantum well, it reduces the peak of the line shape regardless of the intensity. The interesting point is that the electric field decrease the degree of the asymmetry of the absorption line shape. When Δz is increased, it makes the line shape more asymmetric and the effects

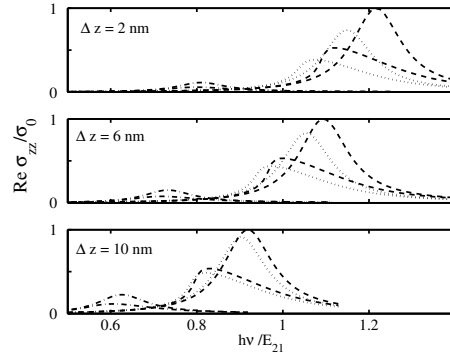


Figure 7.9: The real part of the nonlinear conductivity (normalized) as a function of the photon energy (normalized) for the applied electric fields of $F = 0$ kV/cm (dashed line), $F = 50$ kV/cm (dotted line), and $F = 100$ kV/cm (dashed-dotted line). The symmetric curves represents the case $I = 0$. The well width is $L = 500$ Å. E_{21} is the bare transition energy at $L = 500$ Å and $\Delta z = 20$ Å.

of electric field become weaker both on the peak value and the asymmetry. Note that the red-shift induced by the intensity decreases now since α becomes larger when Δz increased (see Fig. 7.4).

The effect of the well width on the nonlinear absorption line shape can be inferred from $L = 400$ Å and $L = 300$ Å. Without electric field, it is clear that the asymmetry is more pronounced (especially when Δz is increased) while the red-shift associated with the applied intensity is slightly modified. The reducing well width decreases the effect of the electric field on the asymmetry and the peak value in a large amount which is seen clearly at $L = 300$ Å. The reason for this is that α is almost unchanged with the changing electric field, as clearly seen in Fig. 7.4 .

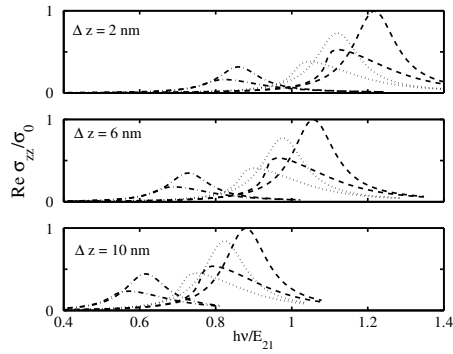


Figure 7.10: The real part of the nonlinear conductivity (normalized) as a function of the photon energy (normalized) for the applied electric fields of $F = 0$ kV/cm (dashed line), $F = 50$ kV/cm (dotted line), and $F = 100$ kV/cm (dashed-dotted line). The symmetric curves represents the case $I = 0$. The well width is $L = 400$ Å. E_{21} is the bare transition energy at $L = 400$ Å and $\Delta z = 20$ Å.

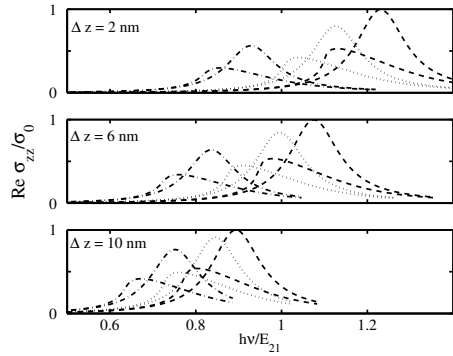


Figure 7.11: The real part of the nonlinear conductivity (normalized) as a function of the photon energy (normalized) for the applied electric fields of $F = 0$ kV/cm (dashed line), $F = 50$ kV/cm (dotted line), and $F = 100$ kV/cm (dashed-dotted line). The symmetric curves represents the case $I = 0$. The well width is $L = 300$ Å. E_{21} is the bare transition energy at $L = 300$ Å and $\Delta z = 20$ Å.

The evolution of the line shape with the changing intensity has not been displayed although we have calculated it. The peak position moves to the lower energy values and peak value diminishes with the increasing intensity while the line shape becomes more asymmetric. In fact, the absorption decreases with the increasing intensity for $\hbar\omega < \overline{E}_{21}$ while it experiences a maximum at some value of I [14]. The quoted results calculated in the absence of the electric field are in agreement with the experimental observations of Sherwin *et al.* [115] and Craig *et al.* [116].

We have calculated the nonlinear intersubband absorption spectra of a Si δ -doped GaAs QW under an electric field for various well widths and sheet thicknesses. We include the depolarization and exciton shifts properly. Contribution of the exciton shift to the intersubband transition energy is proved to be negligible while that of the depolarization shift is not. The effect of the depolarization shift on the nonlinear absorption spectra is solely a blueshift of the transition energy at zero intensity of the incident field. However, when the intensity is increased the absorption line shape becomes strongly asymmetrical and the transition energy is redshifted with respect to the case in which the intensity is zero. At relatively high electric field ($F > 50$ kV/cm), that asymmetry and redshift are significantly reduced when the L is larger ($L \geq 400$ Å). We show that inclusion of the depolarization shift in calculation of the linear and nonlinear absorption spectra can not be ignored in such structures. This could be important for the nonlinear

absorption of nanodevices in the THz range.

CHAPTER 8

CONCLUSION

In this thesis, we have studied the several nonlinear optical properties associated with the intersubband transitions within a semiconductor quantum well described by a Pöschl-Teller type confining potential and the nonlinear intersubband absorption coefficient of a Si- δ -doped GaAs quantum wells. The intersubband transitions in a semiconductor quantum well occur in the technologically important range around $10\ \mu m$ and the oscillator strength associated with these intersubband transitions are extremely large which in turn brings about considerably large nonlinearities in the optical responses of the wells. The semiconductor quantum wells, thus, have potential device applications some of which have been realized, such as quantum well infrared detectors, cameras, emitters, quantum cascade lasers etc. Asymmetry plays an important role in the nonlinear optics. Because, second-order nonlinearities, like second-harmonic generation and the optical rectification, become available with the introduced asymmetry which provides the

break-down of the selection rules while only the third-order nonlinearities are observed previously. Besides, it is possible to establish equally spaced energy levels in the quantum well by adjusting its asymmetry as the resonance cases yield huge values of optical nonlinearities. An asymmetric quantum well is obtained in several ways: either by applying an electric field along the growth direction, or by the band-gap engineering (like step quantum well, or coupling two or more quantum wells with different widths by thin barriers). While these quantum wells have proved fruitful, they have had fixed, not flexible asymmetry property. Pöschl-Teller potential, however, has an adjustable asymmetry property through a set of its parameters. Thus, with such a potential, we have a chance to investigate the effects of the asymmetry on the nonlinear optical properties.

In the first part of the thesis, we have investigated several nonlinear optical properties associated with the intersubband transitions in a quantum well described by the Pöschl-Teller potential. The expressions for the nonlinear optical properties have been obtained through density matrix equation solved by perturbation methods. The resultant expressions are applied to the Pöschl-Teller quantum well and the effects of the asymmetry on the nonlinearities have been investigated by varying its parameters. Any increase in one or both of the parameters, i.e. κ and η , makes the quantum well narrower, while the reverse makes it larger. Second-harmonic generation for a three-level system has been calculated for various values of the asymmetry parameters under a static electric field. The

maximum value of SHG is obtained when one the parameters is largest while the other one is smallest. Because, as the parameters get close to the each other the well becomes more symmetric. The electric field applied in the growth direction enhances the resultant SHG, especially when the parameters are kept small. An interesting point with the application of an electric field is that the electric field makes SHG disappear at some value, depending upon the current values of κ and η . A similar behavior is observed in an asymmetrically coupled quantum well. The resultant SHG is about one order of magnitude larger than one obtained in bulk GaAs. While this is so, it is much smaller than those obtained in experiments held in GaAs/AlGaAs quantum wells or in theoretical studies concerning the GaAs/AlGaAs quantum wells. The main reasons behind that are the nonexistence of the double resonance (i.e. the condition of $E_{10} \cong E_{21}$) and the small electron separation between the ground and the first excited state (i.e. $z_{11} - z_{00}$). We have calculated also optical rectification in the same quantum well. The system is regarded as a two-level system. The result is promising: it is about three order of magnitude larger than the one obtained in bulk GaAs, while it is small compared to those obtained in similar quantum well systems. A further enhancement is possible with the application of an electric field in the growth direction. In all cases, the maximum OR is possible when one the parameters is largest while the other one is smallest. Similar to the case in the calculations of SHG, OR disappears at some value of the electric field which depends upon

values of κ and η .

Third-order nonlinearities are also investigated in our potential through varying its variables. The intensity-dependent absorption coefficient, or the nonlinear absorption coefficient, is considered as a function of the saturation intensity. The saturation intensity is observed to increase at the larger values of κ and η (note that $I_s \sim \mu_{10}^{-2}$). Therefore a better absorption property is possible when the parameters are kept larger. The effect of the electric field is not so much as expected because μ_{10}^2 does not enhance too much for $F < 300$ kV/cm. However, a blue- or red-shift of the absorption peak is possible, depending upon the relative sizes of κ and η . We have calculated also third-harmonic generation for various values of the asymmetry parameters under an electric field regarding the first four energy levels in the quantum well. THG is found to increase as κ and η increase. The addition of electric field makes THG increase further. However, the results are not promising: they are well below those obtained in the experimental and the relevant theoretical works. The main reason for this is the absence of the triple resonance which is the consequence of the equally spaced-energy levels. Finally, we have investigated the intensity-dependent refractive index in a Pöschl-Teller quantum well as a third-order nonlinearity. The peak value of the refractive index is a function of the intensity and the μ_{10}^2 , ($\mu_{10}^2 \sim L^2$) where L is the width of the well. Hence, it is observed to decrease at narrow quantum wells provided that the intensity is constant. We have observed this trend in our

quantum well by varying κ and η because the larger the parameters the narrower the well. The electric field does not affect the refractive index considerably. A reasonable change with the electric field is observable for only smaller values of the parameters. Our findings are in accord with the results of the experimental and the other relevant theoretical works. With recent progress in the fabrication technology, it seems possible to grow semiconductor quantum wells described by the Pöschl-Teller type confining potential. Then the calculations done may help to stimulate the experimental studies, regarding the optical properties, on such quantum wells.

In the second part of the thesis, we have concentrated on the nonlinear intersubband absorption of Si- δ doped GaAs quantum well bounded by infinite barriers. In the literature, there are plenty amount of works on the electronic structure of this type of quantum wells. However, there are a few works on their intersubband absorption properties and all are linear properties. Even though, effects of the Coulomb interaction among electrons in these quantum wells on the absorption spectra is important, few of the works mentioned above took it into account. Thus, by calculating the nonlinear intersubband absorption coefficient of Si- δ doped GaAs quantum wells and including the effect of the Coulomb interaction on the absorption coefficient (i.e. depolarization shift), we have completed a missing but important part. The results are interesting: the blue-shift in the absorption lineshape due to the depolarization shift is reduced by increasing the

intensity of the light and also the absorption lineshape becomes strongly asymmetric degree of which is determined by the strength of the depolarization shift, controllable through the doping density and thickness of the doped sheet, and the intensity of the light. The effects of the electric field on the absorption lineshape are to decrease the peak value and the degree of the asymmetry. In other words, the electric field restores the symmetry of the absorption line shape at larger well widths and thinner doping layers, but it decreases the peak value of the line shape. In conclusion, we show that the intersubband absorption of a Si- δ doped GaAs quantum well at the intensities, close to saturation intensity, shows a strong nonlinearity and the inclusion of the depolarization shift brings about many interesting and new results, which can not be ignored in such structures. These could be important for the nonlinear absorption of nanodevices in the THz range. The calculations may be extended to the other type of nonlinearities, like SHG and THG, and the effects of the Coulomb interaction on them in Si- δ doped GaAs quantum wells and the effects of the finite barrier height may be taken into account.

REFERENCES

- [1] R. Dingle, W. Wiegmann and C. Henry, Phys. Rev. Lett. **33**, 827 (1974).
- [2] L. C. West and S. J. Eglash, Appl. Phys. Lett. **46**, 1156, (1985).
- [3] L. Esaki and H. Sakaki, IBM Techn. Disclosure Bull. **20**, 2456, (1977).
- [4] J. S. Smith, L. C. Chiu, S. Margalit, A. Yariv and A. Y. Cho, J. Vac. Sci. Tech. B **1**, 376, (1983).
- [5] H. C. Liu and F. Capasso, *Intersubband transitions in quantum wells: Physics and device applications I*, Academic Press, San Diego, 2000.
- [6] P. A. Franken, A. E. Hill, C. W. Peters and G. Weinreich, Phys. Rev. Lett. **7**, 118, (1961).
- [7] T. H. Maiman, Nature **187**, 493, (1960).
- [8] M. K. Gurnick and T. A. DeTemple, IEEE J. Quantum Electron. **QE-19**, 791, (1983).
- [9] M. M. Fejer, S. J. B. Yoo, R. L. Byer, A. Harwit and J. S. Harris, Phys. Rev. Lett. **62**, 1041, (1989).
- [10] J. B. Khurgin, Semicond. Semimetals **59**, 1, (1999).
- [11] G. Almogly and A. Yariv, J. Nonlin. Opt. Phys. **4**, 401, (1995).
- [12] C. Gmachl, A. Belyanin, D. L. Sivco, M. L. Peabody, N. Owschimikow, A. M. Sergent, F. Capasso and A. Y. Cho, IEEE J. Quantum Electron. **39**, 1345, (2003).
- [13] E. Rosencher and P. Bois, Phys. Rev. B **14**, 11315, (1991).
- [14] M. Załuźny, Phys. Rev. B **47**, 3995 (1993).
- [15] G. Bastard, *Wave Mechanics Applied to Semiconductor Heterostructures*, Les Editions de Physique, France, 1988.
- [16] J. H. Davies, *The Physics of Low-dimensional Semiconductors: An Introduction*, Cambridge University Press, USA, 1999.

- [17] M.J. Kelly, *Low-Dimensional Semiconductors: Materials, Physics, Technology*, Oxford University Press, New York, 1995.
- [18] H. C. Liu, J. Appl. Phys **73**, 3062 (1993).
- [19] A. Ya. Shik, Sov. Phys. Semicond. **26**, 549 (1992).
- [20] J. J. Harris, J. Mater. Sci.: Mater. Electron. **4**, 93 (1993).
- [21] N. W. Ashcroft and N. D. Mermin, *Solid State Physics*, Holt, Rinehart and Winston, Great Britain, 1976.
- [22] M. H. Degani, Phys. Rev. B **44**, 5580 (1991).
- [23] R. W. Boyd, *Nonlinear Optics*, Academic Press, San Diego, 2003.
- [24] N. Bloembergen, *Nonlinear Optics*, World Scientific, Singapore, 1996.
- [25] Y. R. Shen, *The Principles of Nonlinear Optics*, John Wiley & Sons, USA, 2003.
- [26] G. Pöschl and E. Teller, Z. Physik **83**, 143, (1933).
- [27] S. Flügge, *Practical Quantum Mechanics I*, Springer-Verlag, Berlin Heidelberg, 1971.
- [28] M. M. Nieto, Phys. Rev. A **17**, 1273, (1978).
- [29] H. Yildirim and M. Tomak, Eur. Phys. J. B **50**, 559, (2006).
- [30] D. Ahn and S. L. Chuang, Appl. Phys. Lett. **49**, 1450, (1986).
- [31] B. Y. Tong and N. Kiriushcheva, Phys. Lett. A **229**, 49, (1997).
- [32] B. Y. Tong, Solid State Communications **104**, 679, (1997).
- [33] J. Radovanović and V. Milanavić and Z. Ikonić and D. Indjin , Phys. Lett. A **269**, 179, (2000).
- [34] E. Rosencher, P. Bois, J. Nagle and S. Delaitre, Elect. Lett. **25**, 1063, (1989).
- [35] P. Boucaud, F. H. Julien, D. D. Yang, J.-M. Lourtioz, E. Rosencher, P. Bois and J. Nagle, Appl. Phys. Lett. **57**, 215, (1990).
- [36] C. Sirtori, F. Capasso, D. L. Sivko, S. N. G. Chu and A. Y. Cho, Appl. Phys. Lett. **59**, 2302, (1991).

- [37] C. Sirtori, F. Capasso, D. L. Sivko, S. N. G. Chu and A. Y. Cho, Appl. Phys. Lett. **60**, 151, (1992).
- [38] C. Sirtori, F. Capasso, J. Faist, L. N. Pfeifer and K. W. West, Appl. Phys. Lett. **65**, 445, (1994).
- [39] J. Khurgin, Appl. Phys. Lett. **51**, 2100, (1987).
- [40] J. Khurgin, Phys. Rev. B **38**, 4056, (1988).
- [41] J. Khurgin, J. Opt. Soc. Am. B **6**, 1673, (1989).
- [42] L. Tsang, D. Ahn and S. L. Chuang, Appl. Phys. Lett. **52**, 697, (1988).
- [43] L. Tsang, S. L. Chuang and S. M. Lee, Phys. Rev. B **41**, 5942, (1990).
- [44] Z. Ikonic, V. Milanovic and D. Tjapkin, IEEE J. Quantum Electron. **25**, 54, (1989).
- [45] F. Capasso, C. Sirtori and A. Y. Cho, IEEE J. Quantum Electron. **30**, 1313, (1994).
- [46] S. Tomic and V. Milanovic and Z. Ikonic, Phys. Rev. B **56**, 1033, (1997).
- [47] G. Goldoni, J. Appl. Phys. **89**, 1755, (2001).
- [48] R. Atanasov, F. Bassani and V. M. Agranovich, Phys. Rev. B **50**, 7809, (1994).
- [49] P. Boucaud, F. H. Julien, D. D. Yang and J. M. Lourtioz, Opt. Lett. **16**, 199, (1991).
- [50] Z. Chen, M. Li, D. Cui, H. Lu and G. Yang, Appl. Phys. Lett. **62**, 1502, (1993).
- [51] M. K. Gurnick and T. A. DeTemple, Phys. Rev. A **24**, 1950, (1981).
- [52] P. Boucaud and F. H. Julien, J. Phys. III **1**, 13, (1991).
- [53] J. R. Meyer, C. A. Hoffman, F. J. Bartoli, E. R. Youngdale and L. R. Ram-Mohan, IEEE J. Quantum Electron. **QE-31**, 706, (1995).
- [54] E. Rosencher, J. Appl. Phys. **73**, 1909, (1993).
- [55] G. Almogly and A. Yariv, Opt. Lett. **19**, 1828, (1994).
- [56] I. Vurgaftman, J. R. Meyer and L. R. Ram-Mohan, IEEE J. Quantum Electron. **32**, 1334, (1996).

- [57] W. W. Bewley, C. L. Felix, J. J. Plombon, M. S. Sherwin, M. Sundaram, P. F. Hopkins and A. Gossard, *Phys. Rev. B* **48**, 2376, (1993).
- [58] J. N. Heyman, K. Craig, B. Galdrikian, M. S. Sherwin, K. Campman, P. F. Hopkins, S. Fafard and A. Gossard, *Phys. Rev. Lett.* **72**, 2183, (1994).
- [59] M. Załużny, *Phys. Rev. B* **51**, 9757, (1995).
- [60] V. Bondarenko and M. Załużny, *Physica E* **7**, 212, (2000).
- [61] E. Rosencher, P. Bois, J. Nagle, E. Costard and S. Delaitre, *Appl. Phys. Lett.* **55**, 1597, (1989).
- [62] Y. Huang, C. Wang and C. Lien, *IEEE J. Quantum Electron.* **31**, 1717, (1995).
- [63] E. Rosencher, Ph. Bois, B. Vinter, J. Nagle and D. Kaplan, *Appl. Phys. Lett.* **56**, 1822, (1990).
- [64] K. Unterrainer, J. N. Heyman, K. Craig, B. Galdrikian, M. S. Sherwin, K. Campman, P. F. Hopkins and A. Gossard, *Superlattices and Microstructures* **17**, 159, (1995).
- [65] D. P. Dave, *Electron. Lett.* **28**, 1603, (1992).
- [66] S. Tomic and V. Milanovic and Z. Ikonc, *Optics Communications* **143**, 214, (1997).
- [67] J. Radovanović, V. Milanavić, Z. Ikončić and D. Indjin, *Semicond. Sci. Technol.* **17**, 716, (2002).
- [68] K. X. Guo and S. W. Gu, *Phys. Rev. B* **47**, 16322, (1993).
- [69] H. Yildirim and M. Tomak, *Phys. Rev. B* **72**, 115340, (2005).
- [70] H. Yildirim and M. Tomak, *J. Appl. Phys.* **99**, 093103, (2006).
- [71] S. Y. Yuen, *Appl. Phys. Lett.* **43**, 813, (1983).
- [72] D. Ahn and S. L. Chuang, *J. Appl. Phys.* **62**, 3052, (1987).
- [73] D. Ahn and S. L. Chuang, *IEEE J. Quantum Electron.* **QE-23**, 2169, (1987).
- [74] M. Załużny, *J. Appl. Phys.* **74**, 4716, (1993).
- [75] A. Harwitt and J. S. Harris, *Appl. Phys. Lett.* **50**, 685, (1987).

- [76] G. Bastard, E. E. Mendez, L. L. Chang and L. Esaki, Phys. Rev. B **28**, 3241, (1983).
- [77] D. Ahn and S. L. Chuang, Phys. Rev. B **34**, 9034, (1987).
- [78] D. Ahn and S. L. Chuang, Phys. Rev. B **35**, 4149, (1987).
- [79] D. Walrod, S. Y. Auyang, P. A. Wolff and M. Sugimoto, Appl. Phys. Lett. **50**, 273, (1991).
- [80] C. Sirtori, F. Capasso, D. L. Sivco and A. Y. Cho, Phys. Rev. Lett. **68**, 1010, (1992).
- [81] C. Lien, Y. Huang and J. Wang, J. Appl. Phys. **76**, 1008, (1994).
- [82] Y. Huang and C. Lien, J. Appl. Phys. **75**, 3223, (1994).
- [83] M. Załuźny V. Bondarenko, J. Appl. Phys. **79**, 6750, (1996).
- [84] S. L. Chuang and D. Ahn, J. Appl. Phys. **65**, 2822, (1989).
- [85] K. L. Kuhn, G. U. Iyengar and S. Yee, J. Appl. Phys. **70**, 5010, (1991).
- [86] E. J. Roan and S. L. Chuang, J. Appl. Phys. **69**, 3249, (1991).
- [87] D. P. Dave, J. Appl. Phys. **74**, 6872, (1993).
- [88] J. B. Khurgin and S. Li, Appl. Phys. Lett. **62**, 126, (1993).
- [89] S. Li and J. B. Khurgin, J. Appl. Phys. **73**, 4367, (1993).
- [90] M. V. Marquezini, J. Tignon, T. Hasche and D. S. Chemla, Appl. Phys. Lett. **73**, 2313, (1998).
- [91] F. Inuzuka, K. Misawa, K. Nishi and R. Lang, Appl. Phys. Lett. **85**, 3678, (2004).
- [92] G. H. Wang, Q. Guo and K. X. Guo, Chinese J. Phys. **41**, 296, (2003).
- [93] L. Zhang and J. J. Shi, phys. stat. sol. (b) **242**, 1001, (2005).
- [94] L. Zhang, Superlattices and Microstructures **37**, 261, (2005).
- [95] H. S. Loka, S. D. Benjamin and P. W. E. Smith, Optics Communications **155**, 206, (1998).
- [96] F. Ganikhanov, K. C. Burr, D. J. Hilton and C. L. Tang, Phys. Rev. B **60**, 8890, (1999).

- [97] S. Gehrsitz, F. K. Reinhart, C. Gourgon and N. Herres, J. Applied Phys. **87**, 7825, (2000).
- [98] N.Schwarz et al., Semicond. Sci.Technol. **4**, 571 (1989).
- [99] G. Abstreiter, R. Merlin, and A. Pinczuk, IEEE J. Quantum Electron. **QE-22**, 1771 (1986).
- [100] A. C. Maciel et al., Surf. Sci.**228**, 251 (1990).
- [101] J. Wagner, A. Fischer and K. Ploog, Phys. Rev. B **42**, R7280 (1990).
- [102] A. Zrenner, F. Koch, and K. Ploog, Surf. Sci. **196**, 671 (1988).
- [103] F.Koch and A.Zrenner, Mater. Sci. Eng. B **1**, 221 (1989).
- [104] A. Zrenner et al., Semicond. Sci. Technol. **3**, 1203 (1988).
- [105] M. Santos et al., Mater. Sci. Eng. B **53**, 2504 (1988).
- [106] L.Ioriatti, Phys. Rev. B **41**, 8340 (1990).
- [107] F. A. Reboledo and C. R. Proetto, Solid State Communications **81**, 163 (1992).
- [108] D. Ahn, Phys. Rev. B **48**,7981 (1993).
- [109] F.Dominguez-Adame, B. Mendez, and E. Marcia, Semicond. Sci. Technol. **9**, 263 (1994).
- [110] J. A. Cuesta, A. Sanchez, and F. Dominguez-Adame, Semicond. Sci. Technol. **10**, 1303 (1995).
- [111] A. B. Jazia et al., Semicond. Sci. Technol. **12**, 1388 (1997).
- [112] E.Ozturk and I.Sokmen, Solid State Communications **126**, 605 (2003).
- [113] R. Sasagawa et al., Appl. Phys. Lett. **72**, 719 (1998).
- [114] H. Yıldırım and M. Tomak, phys. stat. sol. (b), to be published.
- [115] M. S. Sherwin et al., Physica D **83**, 229 (1995).
- [116] K.Craig et al., Phys. Rev. Lett. **76**, 2382 (1996).
- [117] L. Hedin and B. I. Lundqvist, J. Phys. C: Solid State Phys. **4**, 2064 (1971).
- [118] W. L. Bloss, J. Appl. Phys. **66**, 3639 (1989).

- [119] T. Ando, A. B. Fowler, and F. Stern, *Rev. Mod. Phys.* **54**, 437 (1982).
- [120] J. P. Hagon, M. Jaros, and D. C. Herbert, *Phys. Rev. B* **40**, 6420 (1989).

CURRICULUM VITAE

PERSONAL INFORMATION

Surname, Name: Yıldırım, Hasan

Nationality: Turkish (TC)

Date and Place of Birth: 2 February 1977, Gaziantep

Phone: +90 312 210 43 35

email: hasany@newton.physics.metu.edu.tr

EDUCATION:

High School: Mimar Sinan Lisesi, Gaziantep, 1994

B.S.: METU, The Faculty of Education, Department of The Science Education, Physics Education Programme, June 1999.

M.Sc: METU, The Graduate School of Natural and Applied Sciences, Physics, June 2001.

PUBLICATIONS

1. H. Yıldırım and M Tomak, “Nonlinear Optical Properties of a Pöschl-Teller Quantum Well”, Phys. Rev. B 72 (2005) 115341-115346.
2. H. Yıldırım and M Tomak, “Intensity-Dependent Refractive Index of a Pöschl-Teller Quantum Well”, J. Appl. Phys. 99 (2006) 093103.

3. H. Yıldırım and M Tomak, “Optical Absorption of a Quantum Well with an Adjustable Asymmetry under an Electric Field”, European Physical Journal B 50 (2006) 559.
4. H. Yıldırım and M Tomak, “Nonlinear Optical Intersubband Absorption of Si δ -Doped GaAs Quantum Well Under an Electric Field”, to be published in Phys. Stat. Sol. B.